



1 **Multi-year black carbon observations and modeling close to the largest**
2 **gas flaring and wildfire regions (Western Siberian Arctic)**

3 **Olga B. Popovicheva¹, Marina A. Chichaeva², Nikolaos Evangeliou^{3,*}, Sabine Eckhardt³,**
4 **Evangelia Diapouli⁴, and Nikolay S. Kasimov²**

5

6 ¹SINP, Lomonosov Moscow State University, 119991 Moscow, Russia

7 ² Faculty of Geography, Lomonosov Moscow State University, 119991 Moscow, Russia

8 ³NILU, Department for Atmospheric & Climate Research (ATMOS), 2007 Kjeller, Norway

9 ⁴ERL, Institute of Nuclear and Radiological Science & Technology, Energy & Safety, NCSR
10 Demokritos, 15341 Attiki, Athens, Greece

11 * Corresponding author: N. Evangeliou (Nikolaos.Evangeliou@nilu.no)

12

13



14 **Abstract**

15 The influence of aerosols on the Arctic system remains associated with significant uncertainties,
16 particularly concerning black carbon (BC). The polar aerosol station "Island Bely", located on Bely
17 Island (Kara Sea) in the Western Siberian Arctic, was established to enhance aerosol monitoring in
18 the Arctic. Continuous in-situ measurements from 2019 to 2022 revealed the long-term effects of
19 light-absorbing carbon. During the cold period, the annual average light absorption coefficient was
20 $0.7 \pm 0.7 \text{ Mm}^{-1}$, decreasing by approximately 2-3 times during the warm period. The interannual
21 mean showed a peak in February ($0.9 \pm 0.8 \text{ Mm}^{-1}$), a ten times lower minimum in June, and exhibited
22 high variability in August ($0.7 \pm 2.2 \text{ Mm}^{-1}$). The absorption Ångström exponent indicated presence
23 of mixed and aged BC. An increase of up to 1.5 at shorter wavelengths from April to September
24 suggests contribution from light absorbing brown carbon. The annual mean *eBC* demonstrated
25 considerable interannual variability, with the lowest in 2020 ($24 \pm 29 \text{ ng m}^{-3}$). Significant difference
26 was observed between Arctic haze and Siberian wildfire periods, with record-high pollution levels in
27 February 2022 ($110 \pm 70 \text{ ng m}^{-3}$) and August 2021 ($83 \pm 249 \text{ ng m}^{-3}$). During the cold season, 92%
28 of surface BC was attributed to anthropogenic sources, mainly from gas flaring. In contrast, during
29 the warm period, Siberian wildfires contributed to BC concentrations by 47%. Notably,
30 unprecedented smoke was transported from Yakutian wildfires at high altitudes in August 2021,
31 marking the most severe fire season in the region over the past four decades.

32

33



34 1 Introduction

35 Multiple socio-economic drivers and feedbacks, including air pollution (Arnold et al., 2016)
36 influence the natural and human environment of the Arctic. Over the last few decades, the Arctic
37 warms more than three times faster than the global average (AMAP, 2021). The pronounced rapid
38 changes affect atmospheric transport and aerosol relative source contributions (Heslin-Rees et al.,
39 2020). Drier conditions and warmer temperatures are the main cause of enhanced fire activity. Boreal
40 forest fires become more frequent and severe (Rogers et al., 2020), especially in Central Siberia, and
41 Northern America (Kasischke and Turetsky, 2006; Kharuk and Ponomarev, 2017; Veraverbeke et al.,
42 2017). Widespread smoke plumes, particularly in Siberia, lead to substantial deterioration of air
43 quality increasing fine particulate matter (Silver et al., 2024).

44 Complicated processes affect Arctic pollution and its climate impacts (Willis et al., 2018), such
45 as the “Arctic haze” in winter and spring. To understand such phenomena and thus reduce their
46 impact, there is a clear need for comprehensive studies of the climate-relevant aerosol processes that
47 occur in the Arctic. A species of major concern is black carbon (BC), a short-lived climate forcer
48 (Schmale et al., 2021). BC is emitted from the incomplete combustion of fossil fuel and biomass; it
49 is defined as the portion of carbonaceous aerosols, which absorb strongly in the entire climate relevant
50 wavelength region of the solar spectrum (i.e. IR-VIS-UV). BC contributes to Arctic warming in
51 multiple ways (e.g., Lee et al., 2013), including the darkening effect of BC deposited on snow and
52 ice (Flanner, 2013). AMAP (2015) reports that the Arctic equilibrium temperature response is
53 (+0.4°C) due to forcing from atmospheric BC and (+0.22°C) due to snow BC.

54 At present, the largest uncertainties when assessing aerosol impact on the climate are attributed
55 to BC (AMAP, 2021). To follow-up on this, BC measurements are taken at various polar regions in
56 the European, Siberian, and Canadian Arctic (Stone et al., 2014; Yttri et al., 2014; Popovicheva et al.,
57 2019a; Winiger et al., 2019; Manousakas et al., 2020; Gilardoni et al., 2023). For instance,
58 Stathopoulos et al. (2021) reported on the long-term impact of light-absorbing carbon in the high
59 Arctic by analysing 15 years of data from the Zeppelin station (Svalbard), while Schmale et al. (2022)
60 studied the status of the Arctic haze peak concentrations at 10 Arctic observatories.

61 There is a large diversity in magnitude and variability of aerosol optical properties, reflecting
62 differences in sources throughout the Arctic (Schmeisser et al., 2018). The most complicated issue
63 for BC measurements is various instrumentations and methods that increase uncertainty (Sharma et
64 al., 2017; Asmi et al., 2021; Ohata et al., 2021). The optical properties of BC have been previously
65 evaluated against direct mass measurements techniques (Sharma et al., 2004; Eleftheriadis et al.,
66 2009; Yttri et al., 2024). The conversion of light attenuation to absorbing carbon mass concentration
67 is performed by the mass-specific absorption coefficient (*MAC*) (Petzold et al., 2013) that is highly



68 influenced by the aerosol mixing state and non-BC light-absorbing species such as organic matter
69 and mineral dust (Zanatta et al., 2018) and varies in time and space depending on sources and
70 transformations during transport (Bond et al., 2013; Chen et al., 2023). It is crucial to quantify the
71 contribution of non-BC component and aging in order to determine the actual *MAC* value
72 experimentally at each site (Singh et al., 2024).

73 The absorption Angstrom exponent, *AAE*, defined as the relative fraction of wavelength -
74 dependence of absorption of BC versus other light absorbing constituents, also differs from site to
75 site (Schmeisser et al., 2018). A fraction of organic aerosol, named brown carbon (BrC), increases
76 the aerosol absorbing properties at short UV-VIS wavelengths (Sandradewi et al., 2008; Grange et
77 al., 2020; Helin et al., 2021) and dominates the absorption during wildfire seasons (Bali et al., 2024).
78 BrC originates mainly from biomass burning and can impose strong warming effect in the Arctic,
79 especially in the summertime (Yue et al., 2022).

80 Despite its remoteness, the Arctic is one of the main receptors of anthropogenic air pollutant
81 emissions from the Northern Hemisphere (Stohl et al., 2013). BC trends and seasonality at three
82 Arctic sites, Alert (Canadian Arctic), Barrow (American Arctic), and Zeppelin, Ny-Ålesund
83 (European Arctic) reveal a negative trend of 40% over 16 years due to the anthropogenic emission
84 reduction (Sharma et al., 2013). The recent increase in fires and their earlier starts, due to the ongoing
85 warming, have made wildfires in the Northern Eurasia a significant source of Arctic BC (Evangelidou
86 et al., 2016). Fossil fuel combustion is the major source of BC in the Arctic troposphere (50–94%)
87 (55–68% at the surface and 58–69% in the snow) and biomass burning (BB) dominates at certain
88 altitudes (600–800 hPa) between April to September (Qi and Wang, 2019).

89 Northern Eurasia, particularly Siberia, is a key source region of pollution in the Arctic. Source
90 quantification (Zhu et al., 2020) shows that surface Arctic BC originates mainly from anthropogenic
91 emissions in Russia (56%). The reason for this is that the largest oil and gas producing facilities of
92 Western Siberia are located along the main pathway of air masses that enter the Arctic and thus have
93 a disproportionately large contribution to the Arctic lower troposphere (Stohl, 2006; Stohl et al., 2013).
94 Eleftheriadis et al. (2009) and Tunved et al. (2013) identified these regions as a key source for the
95 highest measured BC in the European Arctic. The impact of long-range transport from these regions
96 has been previously reported in Ice Cape Baranov station (Manousakas et al., 2020) and Tiksi
97 (Northeastern Siberia) (Winiger et al., 2017; Popovicheva et al., 2019a). Airborne observations over
98 the coast of the Arctic seas have identified the long-term transport of the industrial pollution (Zenkova
99 et al., 2022). Furthermore, efforts have sought to develop BC emission inventories for the Siberian
100 Arctic, based on activity data from local information, improved gas flaring emissions, and satellite
101 data (Huang et al., 2015; Böttcher et al., 2021; Kostrykin et al., 2021; Vinogradova and Ivanova,



102 2023). To better quantify the source contribution to the Arctic environment, targeted aerosol
103 measurements close to the flaring facilities are needed. The present operating Eurasian Arctic stations
104 are all too far away to allow assessing how air masses are affected by different source categories
105 (Stohl et al., 2013). Though, episodic observations of BC at the proximity of the flaring regions have
106 provided a better constraint (Popovicheva et al., 2017b).

107 Another major source of the Arctic BC is wildfires in the Siberian and Far Eastern regions,
108 which have grown in recent summers (Bondur et al., 2020). Airborne observations of BC in Siberia
109 have confirmed impact forest fires (Paris et al., 2009). Eastern Siberia (Yakutia) has been prone to
110 large wildfires due to a combination of hot summers ($> 40^{\circ}\text{C}$) and low humidity (Tomshin and
111 Solovyev, 2022). For instance, wildfires in summer 2019 in Eastern Siberia occurred along the trans-
112 Arctic transport pathway resulting in enhanced aerosol load observed in Western Canada (Johnson et
113 al., 2021). BB emissions occurring at midlatitudes reached the European Arctic in 2020 influencing
114 aerosol composition (Gramlich et al., 2024).

115 Despite the necessity for detailed observations in the Northwestern Siberia, a dense
116 observational network is still absent. Towards this, the polar aerosol station on the Bely Island (Kara
117 Sea, Western Siberia) started to operate in August 2019 (Popovicheva et al., 2022, 2023). The
118 significance of high-quality measurements at the “Island Bely” Station (hereafter “IBS”) is
119 documented, as the station is located along the main pathway of large-scale emission plumes from
120 industrial regions and Siberian wildfires entering the Arctic. Further investigation performed at IBS
121 in August 2021 showed impact from a long-range transport event with unprecedented high
122 concentrations of carbonaceous aerosol (Schneider et al., 2024).

123 In this paper, we show improved light absorption long-term measurements and BC seasonal
124 and inter-annual variability in the Western Siberian Arctic from three and a half years (2019-2022)
125 of observations at IBS. BC was calculated in two ways: as equivalent BC (*eBC*) by an aethalometer
126 and as elemental carbon (EC) by thermal-optical analysis. We further evaluate the seasonal changes
127 in the observed absorption coefficients. Seasonal difference in intensive optical properties is shown
128 by the wavelength-dependent absorption Ångström exponent (*AAE*), which acts as indication of the
129 BrC impact. Estimated site-specific absorption coefficient (*SAC*) considered the specific seasonal
130 effects of mixing and aging of aerosols at IBS. We further assess the inter-annual variability of origin,
131 transport and main BC sources using modelling tools coupled with the most recent anthropogenic and
132 biomass burning emission datasets.



133 2 Methods

134 2.1 Polar aerosol “Island Bely” station (IBS), location and meteorology

135 The aerosol “Island Bely” station (IBS) of Moscow State University (73020'7.57"N,
136 70040'49.05"E) is shown in **Figure 1a** together with other Polar Arctic observatories. Western Siberia
137 is the world's largest gas flaring region with a leading oil and gas production industry (**Figure 1b**). It
138 is also an area under intensive exposure by Siberian wildfires (Tomshin and Solovyev, 2022;
139 Voronova et al., 2022).

140 The climate at IBS is characterized by a large annual variability determined by alternating
141 periods of the polar night and midnight sun. Basic meteorological parameters, such as temperature,
142 wind speed and direction were obtained every 3 hours from a meteorological station located 500 m
143 away from the IBS. The cycles of temperature, precipitation, snow coverage, and wind speed and
144 relative humidity are shown in **Figure S 1**. Annual temperature varied from -39°C to 23°C (mean: -
145 $6\pm 12^\circ\text{C}$) (**Table S 1**). For further analysis, we have split the annual cycle in two periods, November-
146 April (“cold period”) and May - October (“warm period”). High relative humidity of $87\pm 8\%$ was
147 typical for the study period, with less than 80% observed in winter 2020. Precipitation was maximum
148 in summer (22 mm) with constant snow coverage from October to May. Wind was relatively stable,
149 with a mean speed of $6\pm 3\text{ m s}^{-1}$, which increased in winter up to 17 m s^{-1} (**Figure S 1**).

150 Wind pattern for the cold period in **Figure 1d** show a prevailing wind direction from south,
151 southwest, and southeast. Winds were predominantly continental, rarely occurring from the ocean;
152 significant emission sources from the continent were downwind. In the warm period, the wind pattern
153 was more spatially homogeneous with northeastern direction. Period from June and September was
154 characterized by a frequent occurrence of oceanic air masses and constant wind speeds.

155 The aerosol pavilion takes place approximately half a km to the southeast of the meteorological
156 station. An aerosol sampling system composed from three total suspended particle (TSP) inlets has
157 been installed approximately 1.5 m above the roof and 4 m above the ground. They are equipped with
158 an electric heating wire to prevent rimming and ice blocking of the system. One inlet was used for
159 the real-time light-absorption measurements with air flow 5 L min^{-1} . Two other inlets provided the
160 aerosol sampling by low-volume samplers (Derenda, Germany) operating at $2.3\text{ m}^3\text{ h}^{-1}$ flow (0°C ,
161 1013.25 hPa).

162 2.2 Aerosol optical and chemical characterization

163 An Aethalometer model AE33 (Magee Scientific, Aerosol d.o.o.) was used to measure the light
164 attenuation caused by particles deposited on two filter spots at different flow rates (Drinovec et al.,
165 2015) and at seven wavelengths from ultraviolet (370 nm) to infrared (950 nm). The “dual spot”



166 technique is applied for real-time loading effect compensation. Optical absorption of aerosols on the
167 filter is influenced by scattering of light within the filter; the enhancement of optical absorption is
168 described by the factor C that depends on the filter material. The producer recommends an
169 enhancement factor of 1.57 for TFE-coated glass fiber filter. The light-absorbing content of
170 carbonaceous aerosol is reported as equivalent black carbon concentration (eBC_{AET}) for the given
171 wavelength λ , which is determined for each time interval from the change in the light absorption
172 using the mass absorption coefficient (MAC). The aerosol optical absorption coefficient is therefore:

$$173 \quad b_{abs}(\lambda) = eBC_{AET}(\lambda) \times MAC(\lambda) \quad (1)$$

174 where eBC_{AET} at 880 nm is determined using the MAC of 7.7 m² g⁻¹. The aerosol optical absorption
175 coefficient for different wavelengths is determined with their MAC values that are equal to 11.58, and
176 13.14 m² g⁻¹ at 590, and 520 nm, respectively.

177 To represent the spectral dependence of the light absorption, the absorption Ångström exponent
178 (AAE) was derived by using a fitted power law relationship:

$$179 \quad b_{abs}(\lambda) = b_{abs}(\lambda_0) \times \left(\frac{\lambda}{\lambda_0}\right)^{-AAE} \quad (2)$$

180 where $b_{abs}(\lambda_0)$ is the absorption coefficient at the reference wavelength λ_0 , AAE is a measure of
181 strength of the spectral variation of aerosol light absorption.

182 BC absorbs strongly in the NIR-VIS with only moderate increment towards the shorter
183 wavelengths. Light absorbing organic components (BrC) absorb light at shorter wavelengths more
184 effectively than at 880 nm, which is observed as an increased AAE (Sandradewi et al., 2008; Grange
185 et al., 2020; Helin et al., 2021). The total light absorption is assumed to include the contribution of
186 both BC and BrC (Ivančič et al., 2022):

$$187 \quad b_{abs}(\lambda) = b_{abs/BC}(\lambda) + b_{abs/BrC}(\lambda) \quad (3)$$

188 Using Eq. 1, the BrC absorption becomes: $b_{abs/BrC}(\lambda) = b_{abs}(\lambda) - b_{abs}(\lambda_0) \times \left(\frac{\lambda}{\lambda_0}\right)^{-AAE}$ (4)

189 Light-absorption measurements were performed for three and a half years, from 10 August
190 2019 to 31 December 2022, with a time resolution of 1 min. Data were cleaned based on analysis of
191 meteorological parameters by examining whether the wind originated from the direction of the
192 meteorological station where diesel generators operated. In such cases, strong peaks of BC were
193 removed from further analysis. Around 6.4 % of the hourly-average data were cleaned from the
194 dataset due to local pollution impact. To avoid the instrumental noise when calculating the AAE , the
195 z-score was used that calculates the ratio of difference between a single raw data value and the data



196 mean to the data standard deviation. Outliers (< -3 and > 3 of observation's z-score) were removed
197 from the dataset.

198 A thermal EC analysis was conducted for the samples in parallel to AE33. Sampling was
199 performed on 47 mm quartz fiber (Pallflex) filters preheated at 600°C for 5 h. The low concentrations
200 of ambient aerosols necessitate that the sampling times reach up to a week, in order to allow the filter
201 loading to exceed the detection limit for relevant aerosol chemistry analyses. The total number of
202 samples limited by the low detection limit of the thermal-optical instrument were 180.

203 Organic (OC) and elemental carbon (EC) were measured by thermo-optical transmittance
204 (TOT) analysis (Lab OC-EC Aerosol Analyzer, Sunset Laboratory, Inc.) using the methodology
205 reported in Popovicheva et al. (2019) and Manousakas et al. (2020). Quartz filter samples were heated
206 first up to 650 °C in He atmosphere and then up to 850 °C in a mixture of 2% O₂ in He, using the
207 controlled heating ramps of the EUSAAR_2 thermal protocol. OC evolves in inert atmosphere, while
208 the thermal refractory fraction EC is oxidized in the He-O₂ atmosphere. Charring correction due to
209 pyrolytic carbon (PC) was applied by monitoring the sample transmittance throughout the heating
210 process. The limit of detection (LOD) for the EC analysis was 0.05 µg C cm⁻². QA/QC procedures
211 of EN 16909:2017 were also applied during TOT analysis. Laboratory and field blanks were prepared
212 and ran following the same analytical procedures as for the samples.

213 Both methods have important uncertainties (Sharma et al., 2017; Ohata et al., 2021). The
214 determination of EC by thermo-optical analysis may be impacted by the presence of carbonate carbon
215 (CC), which is quantified during analysis as OC and/or EC. The contribution of CC in fine aerosol is
216 generally considered negligible but its interference may be significant for coarse aerosol and samples
217 heavily impacted by resuspended soil. The split between EC and OC may be also affected by the
218 presence of light-absorbing species others than EC, such as light absorbing organic carbon. In
219 addition, the presence of mineral oxides, such as iron oxide, might provide oxygen during analysis
220 and lead to pre-oxidation of EC in inert atmosphere. *eBC* might overestimate BC if there are
221 coexisting components such as BrC (Chakrabarty et al., 2010) and dust (Petzold et al., 2009). In
222 addition, the aethalometer response depends on filter loading and multiple scattering by the filter
223 medium and sampled aerosol particles (Backman et al., 2017).

224 Validations of *eBC* retrievals were performed against results from thermal-optical analysis of
225 EC according to an approach that has been used previously in Sharma et al. (2004), Eleftheriadis et
226 al. (2009) and Yttri et al. (2014). To convert optical absorption at 880 nm to BC mass, the site-specific
227 mass absorption coefficient (*SAC*) was estimated as:

228
$$SAC = \frac{b_{abs/BC}}{EC} \quad (5)$$



229 Data processing was performed using Deming’s total least-squares regression to compare
230 measurements from different methods and modelling, estimate the mass absorption cross-sections
231 (*MAC*), and evaluate correlations among variables (R package “Deming”; (Therneau, 2024)). Deming
232 regression fits a couple of variables considering the independent errors of both. The errors are
233 assumed to be normally distributed; the error ratio is 1, and the regression results are equivalent to
234 the orthogonal regression with the intercept forced through zero.

235 **2.3 Atmospheric dispersion modelling**

236 To investigate the air mass transport and possible origin of BC, the Lagrangian particle
237 dispersion model FLEXPART version 10.4 was used (Pisso et al., 2019) driven by hourly reanalysis
238 meteorological fields (ERA5) from the European Centre for Medium-Range Weather Forecasts
239 (ECMWF) with 137 vertical levels and a horizontal resolution of $0.5^{\circ} \times 0.5^{\circ}$ (Hersbach et al., 2020).
240 In FLEXPART, computational particles were released at heights 0 - 100 m from the receptor (IBS)
241 and tracked backward in time in FLEXPART’s “retroplume” mode. Simulations extended over 30
242 days backward in time, sufficient to include most BC emissions arriving at the station, given a typical
243 BC lifetime of 1 week (Bond et al., 2013). The tracking includes gravitational settling for spherical
244 particles, dry and wet deposition of aerosols (Grythe et al., 2017), turbulence (Cassiani et al., 2015),
245 unresolved mesoscale motions (Stohl et al., 2005), and deep convection (Forster et al., 2007). The
246 FLEXPART output consists of a footprint emission sensitivity that expresses the probability of any
247 emission occurring in each grid-cell to reach the receptor. The footprint can be converted to modelled
248 concentration at the receptor, when coupled with gridded emissions from an emission inventory.
249 Modelled concentrations can be calculated as a function of the time elapsed since the emission has
250 occurred (i.e., “age”), which can be shown as “age spectrum”, while masks of specific
251 regions/continents can give the continental contribution to the simulated concentration (i.e.,
252 “continent spectrum”).

253 The source contribution to receptor BC is calculated by combining each gridded emission sector
254 (e.g. gas flaring, transportation, waste management etc...) from an emission inventory with the
255 footprint emission sensitivity (as described in the previous paragraph). Calculations for anthropogenic
256 sources (emission sectors are described below) and open biomass burning were performed separately.
257 This enabled identification of the exact origin of BC and allowed for quantification of its source
258 contribution. Anthropogenic emissions were adopted from the latest version (v6b) of the ECLIPSE
259 (Evaluating the CLimate and Air Quality ImPacts of ShortlivEd Pollutants) dataset, an upgraded
260 version of the previous version (Klimont et al., 2017). The inventory includes emissions from
261 industrial combustion (IND), from the energy production sector (ENE), residential and commercial
262 emissions (DOM), emissions from waste treatment and disposal sector (WST), transportation (TRA),



263 shipping activities (SHP) and gas flaring emissions (FLR). The methodology for obtaining emissions
264 from FLR specifically over the Russian territories has been improved in ECLIPSEv6 (Böttcher et al.,
265 2021). Annual total and monthly anthropogenic emissions are shown in **Figure S 2**. Biomass burning
266 was adopted from the Copernicus Global Fire Assimilated System (CAMS GFAS) (Kaiser et al.,
267 2012) because this product provides an estimation of the injection altitude of the fire emissions that
268 is crucial for accurate simulation of the BB dispersion. Annual total and daily fire emissions from
269 CAMS GFAS are shown in **Figure S 3**. A satellite image of smoke plume for 5th August 2021 was
270 obtained from <https://worldview.earthdata.nasa.gov>. Fires are shown from the Fire Information for
271 Resource Management System (FIRMS) (<https://firms.modaps.eosdis.nasa.gov/map>) ten days back
272 in time.

273 **3 Results**

274 **3.1 Aerosol light-absorption**

275 Light-absorption coefficients at 880 nm, $b_{abs}(800)$ were used to infer eBC mass
276 concentrations. $b_{abs}(800)$ were plotted as hourly and monthly means during the entire study period
277 (2019-2022) (**Figure 2**). **Table I** presents the data statistical summary. The mean $\pm 1\sigma$ (median) value
278 of $b_{abs}(880)$ was 0.5 ± 0.9 (0.27) Mm^{-1} for the entire study period. In the cold period the annual
279 average mean (median) of $b_{abs}(800)$ was 0.7 ± 0.7 Mm^{-1} (0.5), during the warm period it was 1.9
280 (2.5) times less. There is a clear seasonality consistent with the Arctic aerosol light absorption from
281 other studies (Stathopoulos et al., 2021; Schmale et al., 2022; Pulimeno et al., 2024). 15 years (2001-
282 2015) record at Zeppelin demonstrated that the long-term seasonality of light absorbing carbon
283 (Stathopoulos et al., 2021) $b_{abs}(800)$ was 0.112 Mm^{-1} (median) in the cold period and 0.035 Mm^{-1}
284 in the warm period; both values approximately 5 times less than those observed at IBS.

285 Monthly means of $b_{abs}(800)$ for each year together with intra-annual means for IBS are shown
286 in **Figure 2**. Specifically, annual average $b_{abs}(800)$ exhibits a significant peak during winter and
287 summer for any year. The examination of the overall changes by the inter-annual mean reveals a
288 gradual increase from November (0.4 ± 0.5 Mm^{-1}) to February (0.9 ± 0.8 Mm^{-1}); the latter represents
289 the maximum light absorption observed at IBS. In February, the monthly mean of $b_{abs}(800)$ ranged
290 from 0.4 to 1.7 Mm^{-1} reaching the maximum (1.7 Mm^{-1}) in 2022. Thus, Arctic haze is present at
291 IBS in winter months, from December to February. Starting from March (0.6 ± 0.5 Mm^{-1}), the inter-
292 annual mean decreased down to a minimum in June (0.1 ± 0.2 Mm^{-1}) that was 9 times less than that
293 of February. August had the highest light-absorption (mean: 0.7 ± 2.2 Mm^{-1}) within the summer
294 months, ranging from 0.2 to 1.5 Mm^{-1} and showing a maximum of 1.5 in 2021. September and



295 October demonstrated a similar level of variability with June. The annual monthly mean
296 concentrations for all study years are within $\pm 1\sigma$ of inter-annual mean concentrations (**Table I**) and
297 include 68% of the observed data. At Zeppelin, the maximum of the intra-annual (2001-2015) mean
298 was seen in March - April (0.3 Mm⁻¹) (Stathopoulos et al., 2021), coinciding with the Arctic haze
299 phenomenon in late winter-spring that has been widely observed in the European and Canadian Arctic
300 (Sharma et al., 2004; Schmale et al., 2022).

301 In order to relate the light absorption in visible spectrum to the variability on other locations
302 (Schmeisser et al., 2018; Pulimeno et al., 2024), we calculate b_{abs} at 520 and 590 nm. The mean
303 (median) value of $b_{abs}(520)$ was 0.9 ± 1.6 (0.5) Mm⁻¹ for the entire study period (**Table I**). At Ny-
304 Ålesund (Svalbard), the annual mean (median) $b_{abs}(530)$ averaged for 2018 to 2022 was 0.22 (0.13)
305 Mm⁻¹ (Pulimeno et al., 2024), approximately 4 times less. Moreover, the absorption coefficient
306 $b_{abs}(550)$ of 0.18 (0.09) Mm⁻¹ recorded for 2012-2014 again in Svalbard (Schmeisser et al., 2018)
307 was 4 times less compared to annual average light absorption at IBS.

308 We present multi-annual box-and-whisker plots of b_{abs} at 590 nm in **Figure 3**. The wavelength
309 of 590 nm was chosen as the closest to 550 nm reported for the polar station Tiksi (Schmeisser et al.,
310 2018; Schmale et al., 2022). The monthly medians of $b_{abs}(590)$ in February ranged from 0.3 to 2.3
311 Mm⁻¹, representing the highest values observed in 2022. The highest extended interquartile range
312 (up to 1 Mm⁻¹) was observed in the cold period. Conversely, the summer months exhibited a
313 minimum of approximately 0.1 Mm⁻¹ for $b_{abs}(590)$ with smaller variation of data characterized by
314 the low interquartile range of 0.4 Mm⁻¹.

315 The annual cycle of $b_{abs}(590)$ reflects the higher aerosol burden during the haze season and
316 the low concentrations during summer at Alert, Barrow, Zeppelin, Gruevbadet, and Tiksi (Schmale
317 et al., 2022). Seasonality of b_{abs} medians at 550 nm for polar stations (Alert, Barrow, Tiksi, Zeppelin)
318 from (Schmeisser et al., 2018) and $b_{abs}(590)$ for IBS are presented in **Figure 3**. All sites demonstrate
319 similar seasonal variations, albeit a different magnitude of light absorption. In February, the
320 maximum $b_{abs}(590)$ (1.1 Mm⁻¹) was observed at IBS; a higher value has been only observed at
321 Tiksi which is explained by the influence from local sources (Popovicheva et al., 2019a). Other
322 stations show the Arctic haze maximum later (in March or April); a sharp decline of $b_{abs}(590)$ was
323 observed at those months at IBS. Values similar to other Arctic stations were recorded at IBS in June,
324 with an annual minimum of around 0.1 Mm⁻¹. Since July, $b_{abs}(590)$ at IBS was higher than at other
325 stations except Tiksi and peaked at 0.8 Mm⁻¹ in December. The polar station Pallas exhibits the
326 opposite behaviour peaking in spring and summer (Schmeisser et al., 2018). Pallas is located
327 relatively south as compared to the rest of the polar stations and, hence, it is influenced by
328 anthropogenic and biogenic emissions from surrounding boreal forests (Asmi et al., 2011). Finally,



329 we conclude that at IBS the aerosol optical properties in the IR and visible solar spectrum are different
330 from European, Canadian and Western high-latitude polar locations: light absorption coefficients are
331 higher during the annual cycle as well as Arctic haze is the most prominent in December-February.

332 3.2 Black carbon and site-specific mass absorption cross-section

333 Elemental carbon (EC) collocated with light absorption observations is widely used to infer BC
334 (Grange et al., 2020). **Figure 4a** shows concentrations of EC determined for samples collected in
335 parallel with the aethalometer measurements from 10 August 2019 to 31 December 2022, with
336 eBC_{AET} concentrations averaged over the sampling period. Both weekly EC and eBC_{AET}
337 concentrations show the same seasonal variations with a maximum in winter and minimum in
338 summer. EC concentrations are generally smaller than eBC_{AET} . The annual EC mean concentrations
339 ranged from 6.5 to 16.3 ng C m⁻³. The highest EC (0.2 µg C m⁻³) was recorded in December 2019
340 and the highest eBC_{AET} (0.4 µg m⁻³) in December 2019 and January 2022. EC was higher (0.05±0.03
341 µg C m⁻³) in the cold period and decreased (0.02±0.03 µg C m⁻³) in the warm period (**Table I**).
342 Annual average mean EC during the entire study period was 0.03±0.03 µg C m⁻³. For comparison,
343 at Zeppelin and Villum the annual mean EC concentrations were 0.012 ±0.04 µg C m⁻³ (2017-2020)
344 (Yttri et al., 2024) and 0.029 ±0.03 µg C m⁻³ (2011-2013) (Massling et al., 2015), respectively.

345 Annual mean OC concentrations during the entire study period were estimated as 0.45±0.3 µg
346 C m⁻³. At Zeppelin, annual OC (2017-2020) was 3.5 smaller (0.13±0.1 µg C m⁻³) (Yttri et al., 2024).
347 Notably, the multi-year average EC and OC levels at IBS are approximately 3 times higher than at
348 Zeppelin, that correlates well with increased light absorption, as described previously. At IBS, OC
349 was 0.4±0.2 µg C m⁻³ in the cold period and increased to 0.5±0.4 µg C m⁻³ in warm period, opposite
350 to EC (**Table I**). The ratio OC/EC shows increased OC and decreased EC in the warm period and an
351 opposite trend in the cold (**Figure 4b**). **Figure 4c** depicts the relationship between eBC_{AET} and EC in
352 cold and warm periods. We note the high R² values for the cold period (0.88) and slightly lower ones
353 for the warm one (0.78). During the warm period, seasonal mean values reveal an overestimation of
354 eBC_{AET} that is more pronounced during the warm period, with a slope equal to 2.3. R² values were
355 lower because many EC values were close to the LOD. Seasonal differences are attributed to pollutant
356 sources altering the chemical composition of aerosol at IBS. A positive correlation was observed
357 between eBC_{AET}/EC and OC/EC indicating that BC at IBS is coated with OC leading to the lens effect
358 (Kanaya et al., 2008) and overestimating eBC .

359 Similar seasonal variation for eBC and EC with highest winter and lower summer
360 concentrations has been observed previously at Villum, with a regression slope of 2 and a R² of 0.64
361 (Massling et al., 2015). At Alert, the median SAC during the Arctic haze season (November to April)
362 was 19.8 m² g⁻¹ (Sharma et al., 2004). However, during the non-Arctic haze period from May to



363 October it was significantly higher $28.8 \text{ m}^2 \text{ g}^{-1}$ and much more variable. This is explained by aged,
364 internally mixed, and of anthropogenic origin of winter and spring arctic aerosols while summer
365 aerosols were affected by local sources.

366 Following the definition in Eq.5, we calculate the *SAC* from the slope of BC light absorption at
367 880 nm , $b_{abs/BC}(880)$, and EC concentrations. $SAC_{BC,cold}$ (for the cold period) was estimated to be
368 $15.9 \text{ m}^2 \text{ g}^{-1}$ while $SAC_{BC,warm}$ was higher ($18.1 \text{ m}^2 \text{ g}^{-1}$) (**Figure 5**). *SAC* values at Alert have been
369 reported to be even higher (Sharma et al., 2004), showing that Western Arctic aerosols differ by
370 composition and aging. Recalculations of BC mass with *SAC* values for cold and warm periods (*eBC*),
371 separately, were performed according to Eq.1.

372 Timeseries of daily and monthly mean *eBC* concentrations from August 2019 to 31 December
373 2022 are shown in **Figure 2**. Annual mean and median *eBC* for the entire period were 28.7 ± 54.1
374 ng/m^3 and 12.5 ng m^{-3} , respectively (**Table 1**); they exhibit a strong year-by-year variability. *eBC*
375 climatology and the statistics for each month and year of study are presented in **Figure 2** and **Table**
376 **S 2**. The annual mean *eBC* in 2019, 2021 and 2022 was 33 ± 44 , 33 ± 85 , and $32 \pm 48 \text{ ng m}^{-3}$, respectively.
377 Statistically significant difference at the 95% confidence level with a p-value < 0.05 (t-test) was
378 observed for the cold and warm periods with means 44 ± 47 and $19 \pm 57 \text{ ng m}^{-3}$, respectively. The
379 smallest mean *eBC* of $24 \pm 29 \text{ ng m}^{-3}$ occurred in 2020. The latter is likely attributed to the impact of
380 COVID-19 restriction measures to the emissions of BC (Evangelidou et al., 2020).

381 The general trend of the maximum in winter and minimum in summer well reproduces the
382 typical *eBC* seasonality reported in polar observatories (Stone et al., 2014; Schmale et al., 2022).
383 **Figure 2** shows monthly mean *eBC* concentrations for half of year 2019 and whole - year periods of
384 2020, 2021, and 2022 as well as annual averaged monthly mean *eBC* climatology for the entire study
385 period. The highest concentration in the cold period was observed in December 2019 ($82 \pm 67 \text{ ng m}^{-3}$),
386 January 2022 ($63 \pm 51 \text{ ng m}^{-3}$), February 2022 ($106 \pm 67 \text{ ng m}^{-3}$), and March 2021 ($32 \pm 24 \text{ ng m}^{-3}$)
387 (**Table S 2**). In warm periods we recorded the highest concentrations in September 2020 ($31 \pm 48 \text{ ng}$
388 m^{-3}), August 2021 ($83 \pm 249 \text{ ng m}^{-3}$), April 2021 ($35 \pm 26 \text{ ng m}^{-3}$), and August 2022 ($28 \pm 54 \text{ ng m}^{-3}$).

389 3.3 Multi-wavelength absorption Angstrom exponent

390 As shown by Virkkula (2021), pure BC particles surrounded by non-absorbing coatings can
391 have absorption Angstrom exponent (*AAE*) in the range from < 1 to 1.7 . Compendium of values from
392 different emissions show *AAE* variation from 0.2 to 3.0 for transport, power plants, and domestic
393 wood burning (Helin et al., 2021). Primary emissions from residential heating (Cuesta-Mosquera et
394 al., 2024) and biomass burning (Popovicheva et al., 2017a, 2019b) have been associated with high
395 *AAE* of around $3-4$. Due to the mixing with background aerosol, coating and aging processes, a large



396 change in the light absorption has been reported at receptors of long-range transported pollution
397 (Cappa et al., 2016). For highly aged aerosols, AAE has been found lower than 1.0 due to large and
398 internally mixed particles (Popovicheva et al., 2022). Spectral absorption was obtained at IBS in the
399 UV to IR spectral region emphasized by the value of $AAE_{350/950}$ equal to 0.96 for the entire study
400 period (**Figure 6a**). Power law fittings of spectral dependence for both and cold periods show similar
401 values, indicating highly mixed and aged BC.

402 Multiple studies have addressed the sensitivity of the AAE to the range of wavelengths
403 selected for its calculation (Cuesta-Mosquera et al., 2024); the extent of this sensitivity is higher for
404 aerosols containing a substantial contribution of organic species such as BrC. Events affected by
405 regional fire emissions were evident by the light absorption coefficient $AAE_{370/520}$ in the short
406 wavelength range (Ulevicius et al., 2010). In remote Arctic environments, cases with exceeded
407 $AAE_{467/660}$ have been identified to be influenced by BB (Pulimeno et al., 2024). Impact of intensive
408 wildfires in North America on aerosol optical properties measured at the European Arctic has been
409 associated with increased daily $AAE_{467/660}$ of up to 1.4 (Markowicz et al., 2016). Strong UV
410 absorption has led to increase of up to 1.8, clearly indicating the importance of non-BC light-
411 absorbing component (Ran et al., 2016).

412 To apportion the wavelength-dependent light absorption, we used a pair of wavelengths in the
413 whole wavelength (350 and 950 nm) range, in shorter (370 and 660 nm) and (370 and 520 nm) ranges.
414 Timeseries of weekly average $AAE_{370/520}$ showed a similar seasonality but wider variation (0.2-3.1)
415 than (0.5-1.7) for $AAE_{370/950}$ (**Figure 6b**). The mean values increased from 0.97 ± 0.23 for
416 $AAE_{370/950}$ to 1.17 ± 0.5 for $AAE_{370/520}$ for the entire study period (**Table I**). Box-whisker plots and
417 annual averaged means of $AAE_{370/950}$ showed no prominent monthly dependence (**Figure 4c**).
418 However, increased $AAE_{370/950}$ above 1.1 was observed in summer months for several years, in July
419 2020, June 2021 and from May to September 2022 (**Table S 2**). The shorter the wavelength pair, the
420 higher the annual average AAE above 1.0. The largest values of monthly mean (median) $AAE_{370/520}$
421 were found for April to September with a maximum in June. Such considerable deviation during
422 warm months implies the importance of BrC light-absorbing components within highly mixed Arctic
423 aerosols at IBS.

424 Light absorption at 370 nm, $b_{abs}(370)$, was used to estimate the BrC mass concentrations.
425 The mean (median) value of $b_{abs}(370)$ was 2.4 times higher than $b_{abs}(880)$ for the entire study
426 period as well as for cold and warm ones (**Table I**). Monthly means and box-whisker plot of
427 $b_{abs}(370)$ showed trends similar to $b_{abs}(880)$ (**Figure S 3**). Assuming that the wavelength pair λ
428 and λ_0 in Eq. 3 being 370 and 950 nm, respectively, the absorption coefficient for BrC at 370 nm,



429 $b_{abs/BrC}(370)$, is determined by subtracting BC absorption from the total absorption at the same
430 wavelength using the $AAE_{370/950}$ value for entire period (**Table I**). Monthly $b_{abs/BC}(370)$ and
431 $b_{abs/BrC}(370)$ as well as the $b_{abs/BrC}(370)$ contribution to total $b_{abs}(370)$ are shown in **Table S 3**
432 for those years when the contribution of BrC absorption was higher than 1%. We note 13% for August
433 2021 for the warm period and 5 % for February 2022 and December 2021 for the cold period.

434 **3.4 Modelled concentrations of BC**

435 **Figure 7a** shows the monthly mean eBC and surface BC ($BC_{FLEXPART}$) concentrations
436 simulated with FLEXPART coupled to ECLIPSEv6-GFAS emissions for the entire study period.
437 FLEXPART model performs well in capturing the seasonality of observed features with both high
438 and low concentrations. Annual mean modelled BC (88.4 ng m⁻³) is 37% higher than aethalometer-
439 measured eBC_{AET} (64.3 ng m⁻³) and 3 times higher than eBC (29.5 ng m⁻³). Annual and monthly
440 means of eBC_{AET} show values closer to $BC_{FLEXPART}$ than eBC . This is a reasonable finding because
441 the global emission datasets could not consider local pollution. Almost all simulated BC
442 concentrations, except in February 2020 and 2021, were found within the standard deviation range of
443 measured eBC_{AET} . A good correlation between measurements and simulations, with a Pearson
444 coefficient of 0.72 and 0.7 and a root mean squared error (RMSE) of 15 ng m⁻³ and 0.14 ng m⁻³ was
445 obtained for the cold and warm period, respectively (**Figure 7b,c**).

446 FLEXPART does not reproduces seasonal variations of BC everywhere over the Arctic. R2
447 and RMSE varied between 0.53-0.80 and 15.1-56.8 ng m⁻³, respectively, depending on the location
448 (Zhu et al., 2020). At Zeppelin, modelled BC (annual mean of 39.1 ng/m³) was reported to be 85%
449 higher than the measured value (21.1 ng m⁻³ for annual mean). At Tiksi, modelled BC was
450 underestimated (74.4 ng m⁻³ for annual mean) by 40% compared with observations (104.2 ng/m³ for
451 annual mean) (Zhu et al., 2020). Such good result for IBS is due to its closer location to the biggest
452 emission sources.

453 **Figure 8** shows the vertical distribution of simulated BC as a function of time for 2019-2020
454 years (vertical cross-section). Consistently high vertical BC profiles up to 2 km were observed in the
455 cold period, except in April 2022. In February 2020, a smoke layer of BC concentrations of up to 100
456 ng m⁻³ was prominent at up to 4 km. On the contrary, in the warm period the smoke resides near the
457 surface, despite a few events of extremely high vertical BC at altitudes up to 8 km and 10 km, which
458 occurred in July 2020 and August 2021, respectively. Nevertheless, the evidence of atmospheric
459 transport from high altitudes during summer months is evident by the elevated modelled BC (>100
460 ng m⁻³) at high model layers (e.g., July 2019, June-August 2020, June-July 2021 and May-June
461 2022). In all these periods, surface modelled BC (violet line in **Figure 8**) was under 40 ng m⁻³
462 showing that the emission sources are probably far away, and that long-range transport occurred. The



463 low injection altitude of anthropogenic emissions in winter months cause emitted substances to
464 remain close to the emission sources. BC climatology at IBS indicates that the long-range transported
465 anthropogenic emissions in the cold period reside at altitudes up to 2 km and compose a persistent
466 layer (**Figure 8**). This is further explained by the rapid (about 4 days, or less) low-level transport of
467 air masses to the Arctic troposphere as described in Stohl (2006). However, this cannot be confirmed
468 without targeted high altitude observations.

469 **4 Discussion**

470 **4.1 Long-range transport, age and region contributions**

471 Transport mechanisms from the source regions affect the Arctic BC variability and burden
472 (Chen et al., 2023; Zhou et al., 2012). Transport of aerosols to the Arctic leads to high concentrations
473 of BC in winter and spring (Arctic haze) and low values in summer (Law and Stohl, 2007) when the
474 removal processes in the dry and stable Arctic atmosphere are very slow. Synoptic-scale circulation
475 effects promote the effective transport from lower latitudes, namely diabatic cooling of air masses
476 moving over snow-covered ground, high continental pressure in winter, and the intrusion of warm air
477 from lower latitudes (Gilardoni et al., 2023). Seasonal trends of footprint emission sensitivity
478 demonstrate the transport mechanisms from the source regions to the European Arctic (Platt et al.,
479 2021). BC at Zeppelin is affected by significantly different source regions during the warm and cold
480 seasons, while large-scale circulation patterns that affect the pollutant transport from lower latitudes
481 show the opposite behaviour during these two periods (Stathopoulos et al., 2021).

482 **Figure 9** shows a 3.5-year climatology of the surface footprint emission sensitivities at IBS.
483 From December to February, anthropogenic polluted air mass transportation takes place from Eurasia
484 (territories above 40°N), as illustrated by the elevated footprints there. The extension of the Arctic
485 front towards lower latitudes during the cold period facilitates such transport (Stohl, 2006). The
486 warmer it gets in spring, the narrower the area of emission transport. In the transition from spring to
487 summer, transport patterns and meteorological conditions change, such as that the advection of the
488 particulate pollution to the Arctic boundary layer from lower latitudes becomes limited (Bozem et al.,
489 2019). In JJA (June, July, August) footprint is mostly restricted to coastal regions of Eurasia,
490 Greenland, and North America and does not extend deeply into the continents. This is a consequence
491 of the so-called ‘polar dome’ that prevents warm continental air masses from entering the Arctic
492 lower troposphere (Stohl, 2006). As a result, anthropogenic pollution becomes less significant, and
493 natural aerosol sources prevail (Moschos et al., 2022b, a). In autumn (September, October,
494 November), footprint is similar to the MAM (March, April, May) one completing the annual cycle.



495 For the entire study period, the monthly mean contribution to surface BC for all years was
496 from air masses with 1-3 (31%) and 3-6 days (22%) aging (**Table S 4**). The highest BC contribution
497 (34%) and (39%) was observed for the shortest age of 1-3 days in DJF (December, January, February)
498 and MAM, respectively (**Figure 8**). In summer, the highest BC contribution (35%) was replaced by
499 a longer age of 6-9 days.

500 Footprint emission sensitivities of Arctic air masses also constrain the region contributions.
501 The major source regions contributing BC to IBS are the territory of the Russian Federation (including
502 European part of Russia (EURus), Siberia, Far East), Asia, Europe, Northern America, and Ocean.
503 Due to the geographical proximity, EURus/Siberia/Far East contribution (77%) dominated during the
504 entire study period on a basis of the annual average monthly means (**Table S 4**), with a maximum of
505 83% in SON (**Figure 9**). Its monthly maximum (88%) was recorded in September 2021, and the
506 minimum (60%) in June 2022. Europe was the second region contributor (11%) followed by Asia.
507 The monthly mean contribution of Northern America was up to 12% in JJA, the largest was observed
508 in July 2022 (62%).

509 **4.2 Anthropogenic and biomass burning sources**

510 The time series of monthly mean and annual average monthly mean source contributions to
511 surface BC at IBS are shown in **Figure 10a**. Anthropogenic sources (DOM, TRA, IND, FLR, All
512 others) contribute 83% of the total for the entire study period (**Table S 4**). A decrease from winter to
513 July and an increase from August to winter were seen. In the cold period, air masses arrived at IBS
514 through the populated regions of Western Europe, European part of Russia, Siberia, and Asia,
515 crossing the biggest oil and gas extraction regions of Kazakhstan, Volga-Ural, Komi, Nenets, and
516 Western Siberia (**Figure 1**). Because IBS is located north of the largest oil and gas producing regions
517 of Western Siberia, high FLR contribution of 50% and 32% was observed both in the cold and warm
518 period (**Table S 4**). Annual mean contributions to modelled surface BC from FLR, DOM, TRA, and
519 IND sectors dominated in January and December (60%, 22%, 12%, and 9%, respectively). All other
520 sources were around 2% at that time. BB played the biggest role between April (8%) and October
521 (17%), with maximum in August (80%).

522 **Figure 10b** shows the percentage sectoral contributions on monthly mean BC concentrations
523 for each year. February 2021 and December 2021 were the leaders of FLR impact with 67.2% and
524 67.4%, respectively. During February 2022 of the record high BC pollution level observed at IBS, air
525 masses arrived at IBS through the Western Europe, European part of Russia, and Siberia, passing
526 through the flaring facilities of Kazakhstan, Volga-Ural, Komi, Nenets, and Western Siberia. They
527 caused of 50%, 26%, 15%, 8%, 0.2%, and 3.3% monthly average contribution to surface BC from
528 FLR, DOM, TRA, IND, BB and All other sources, respectively. Footprint emission sensitivities on



529 3rd February 2022 at 12:00-15:00 when *eBC* reached 310 ng m⁻³ (**Figure S 5**) showed air mass
530 transport to IBS straight through the Western Siberian gas flaring region (**Figure 10c**).

531 The contribution of FLR dropped significantly from April to a minimum of 18% in June and
532 rose in September. In the winter months when the overestimation of modelled BC concentrations was
533 recorded (see section 3.4), the highest FLR impact was seen. DOM showed the biggest contribution
534 (18%) from November to February, exactly during the heating season. The light absorption of BrC
535 was significant mostly in wintertime (**Table S 3**). The latter indicates significant impact of biomass
536 used for domestic heating, in accordance to wood burning contribution of 61% of the total residential
537 emissions in forest regions (Huang et al., 2015).

538 According to CAMS GFAS (**Figure S 3**), significant global fire emissions started from June
539 and lasted until the mid of November in 2020 and 2022; the period of fire emissions was shorter but
540 more intensive from July until September 2021. At IBS, the annual mean BB contribution approached
541 48% of the total in the warm season (**Table S 4**). It started increasing from April and approached a
542 maximum of 80% in August, whereas TRA, DOM, IND, and All other sources were minimum. From
543 middle June to September, the average monthly BB contribution was larger than all anthropogenic
544 sources. Notably, from April to September, the high mean BB contribution was related to the excess
545 of $AAE_{370/520}$ over 1.0 (maximum: 1.7 in July) (**Figure 6**). At that time, the air masses transported
546 to IBS were aged (> 6 days) dominating the age spectrum (60%) (**Table S 4**).

547 In 2019, 72.4 thousand km² were burned in Siberia or 42% of the total burned area that
548 occurred in Russia (Voronova et al., 2020). A significant relationship between the burned areas and
549 associated pyrogenic emissions with atmospheric blocking events was reported (Mokhov et al., 2020).
550 August and September showed 50% and 35%, respectively, monthly mean BB contributions, while
551 October and November lower, 30% and 20%, respectively (**Figure 10b**).

552 In spring 2020, BB BC concentrations simulated with WRF-Chem were distributed in areas
553 between 40°N and 60°N in Europe, central Siberia, and East Asia, and indicated intensive seasonal
554 agriculture fires in Europe and Siberia (Chen et al., 2023). Spring fires contributed about 12% BB
555 BC to IBS (April and May). The end of June and beginning of July of 2020 was characterized by high
556 altitude BC (**Figure 8**) indicating high altitude long-range transport. A high BrC content was also
557 observed in July and September 2020 (**Table S 3**).

558 In 2021, the monthly mean spring BB contribution approached a maximum of 36% in May.
559 Yakutia (Eastern Siberia) experienced the worst fire season over the last four decades (Tomshin and
560 Solovyev, 2022). Around 150,000 occurred, almost twice as much as the previous year (Voronova et
561 al., 2022). August 2021 received 90% contribution from BB as compared to all the other sources. At
562 that time unprecedented high smoke levels were recorded over Western Siberia (Schneider et al.,
563 2024). Satellite image reveals the strong plume from the area of Yakutian wildfires which brought



564 deep smoke to IBS located around 2000 km far away (**Figure 1c**). The highest *eBC* level of 1800 ng
565 m⁻³ on 5th August, exceeded the 75th percentile of the entire period 53 times (**Table 1**)! The measured
566 concentrations were 180 times higher than the Arctic background (**Figure S 6**). Severe smoke affected
567 the visibility near IBS (**Figure 1d**). Footprint emission sensitivity on 5th August (from 18:00 to 21:00)
568 at the time when *eBC* peaked (1540 ng m⁻³) confirms that air masses originated from Yakutia and
569 arrived to IBS from the northeast direction (**Figure 10c**). BC for these wildfires was transported at
570 altitude as high as 10 km (**Figure 8**). Finally, in summer 2022, wildfires took place in Western Siberia
571 and the European part of the Russian Federation (Popovicheva et al., 2023); BB contributions in June,
572 July, August 2022 were around 65%, whereas light absorption of BrC was important in May and
573 August 2022 (**Table S 3**).

574 5 Conclusions

575 Almost four years (2019-2022) of observations at the aerosol station IBS highlight the light-
576 absorption characteristics of Western Siberian polar aerosols and its basic cycles, such as seasonality,
577 annual means, and interannual variability. The annual cycle of multi-wavelength light absorption
578 demonstrates higher levels during the Arctic haze season and lower ones in summer, similar to other
579 observatories across the Arctic. The light absorption coefficient revealed a number of unique features:

- 580 • Higher magnitude (around 4-5 times) in comparison with multi-year observations at high-latitude
581 polar stations in European Arctic (annual mean of 0.7 ± 0.7 Mm⁻¹ in the cold season and 2 times
582 lower in warm).
- 583 • Wintertime maximum was observed in February (0.9 ± 0.8 Mm⁻¹) that coincides with the Arctic
584 haze peak; this is different from the European and Canadian Arctic that is usually observed in
585 early spring. The interannual minimum was observed in June whereas August was highly
586 variable with respect to light-absorption due to the Siberian wildfires.
- 587 • Multi-annual monthly means for light absorption coefficients in the visible spectrum at IBS were
588 found higher than at European, Canadian and Western high-latitude polar locations, due to that
589 IBS is closer to the main Northern Eurasian source regions.
- 590 • Wildfire caused increased concentrations, usually in August. Increase of absorption Angstrom
591 exponent in the UV spectrum between April and September implies coexistence of highly
592 mixed/aged BC and light-absorbing BrC components, revealing BB aerosols at IBS. Specifically,
593 monthly BrC contribution to total light absorption was 5 % in February 2022 and 13% August
594 2021 likely due to wildfire impact.
- 595 • BrC light absorption coefficient in the UV spectrum showed similar trends as BC, although it
596 exceeded BC by 2.4 times during both cold and warm periods. AAE was equal to 0.96, indicating



597 highly mixed and aged aerosols. AAE in UV spectrum increase up to 1.17 ± 0.5 implies
598 coexistence of light-absorbing BrC components in biomass burning aerosols, with the biggest
599 impact between April and September.

- 600 • We calculated site-specific mass absorption coefficient (*SAC*) for the first time at IBS by
601 combining multi-year optical absorption and EC data. Higher *SAC* of $18.1 \text{ m}^2 \text{ g}^{-1}$ in the warm
602 period than in the cold one ($15.9 \text{ m}^2 \text{ g}^{-1}$) revealed influence from non-BC light-absorbing
603 species, such as organic matter and mineral dust; *SAC* values were lower than those observed in
604 the Canadian Arctic indicating different aerosol composition and aging.
- 605 • Annual mean *eBC* in 2019, 2021 and 2022 was 33 ± 44 , 33 ± 85 , and $32 \pm 48 \text{ ng m}^{-3}$, respectively.
606 Mean *eBC* in the cold and warm periods were equal to 44 ± 47 and $19 \pm 57 \text{ ng m}^{-3}$, respectively.
607 Record high *eBC* was found in February 2022 ($110 \pm 70 \text{ ng m}^{-3}$) and August 2021 ($83 \pm 249 \text{ ng}$
608 m^{-3}) during the years of study.

609 The relationship between the magnitude of aethalometer-measured *eBC* and thermo-optical
610 EC was evaluated at IBS with respect to the specific atmospheric conditions. *eBC* mass recalculated
611 with site-specific absorption coefficient values indicates the observed seasonal effects and gives an
612 indication of the chemical composition of aerosols. The observed annual cycles show typical Arctic
613 trends with *eBC* concentrations higher in the cold period when transport of air masses to IBS occurs
614 mostly from the European part of Russia, Siberia, Far East, Europe and Asia. When air masses pass
615 through the oil and gas facilities of Kazakhstan, Volga-Ural, Komi, Nenets, and Western Siberia, BC
616 contribution from gas flaring dominates over domestic, industrial, and traffic sectors, with a
617 maximum contribution in January. From June to August, BB source contribution from Siberian fires
618 exceeds the anthropogenic one. August 2021 and February 2022 showed significant differences with
619 respect to annual means. During these months, record high BC pollution levels were observed.
620 August 2021 experienced the worst fire season over the last four decades bringing smoke at IBS.
621 Vertical distribution of BC at IBS shows a persistent low level BC layer in the cold period, and a
622 high altitude wildfire smoke layer in the warm period.

623 Our modelling analyses demonstrate the transport mechanisms from different regions:

- 624 • Around 77% contribution from the European part of Russia, Siberia, and Far East was estimated
625 during the entire study period, followed by Europe (11%), Asia (7%) and North America (4%).
- 626 • From December to February, air mass transport from Eurasia (territories above 40°N), from 1-3
627 days far from IBS took place, whereas in summer the warm continental airmasses travelled 6-9
628 days until they reached the receptor.
- 629 • The low injection altitude of anthropogenic emissions in cold period leads to a persistent vertical
630 BC layer at altitudes up to 2 km, with a record high concentration of 100 ng m^{-3} up to 4 km in



631 February 2020. In warm period the low BC layer is further elevated due to smoke arriving from
632 the numerous Siberian wildfires.

- 633 • Anthropogenic sources contribute 83% of the total for the entire study period; FLR, DOM, TRA,
634 and IND sectors dominate during the Arctic Haze (60%, 22%, 12%, and 9%, respectively).
635 Highest gas flaring (FLR) contribution of 50% and 32% is persistent both in the cold and warm
636 seasons due to the IBS location north of the largest oil and gas producing regions of Western
637 Siberia.
- 638 • DOM showed the largest contribution (18%) during the heating season, in agreement with the
639 enhancement of BrC light absorption due to high wood burning contribution from residential
640 emissions.
- 641 • During February 2022, modelled BC as 310 ng m⁻³ when air masses arrived through Western
642 Europe, European part of Russia, and Siberia, passing through the flaring facilities of
643 Kazakhstan, Volga-Ural, Komi, Nenets, and Western Siberia. The overestimated modelled
644 concentrations are likely a result of miscalculated source intensities during these months.
- 645 • Annual mean BB contribution approached 48% in the warm season, increasing from April and
646 approaching a maximum (80%) in August. From middle June to September, the monthly mean
647 BB contribution was larger than anthropogenic sources. A few extreme events of high vertical
648 BC at altitudes up to 8 km and 10 km occurred in July 2020 and August 2021, respectively,
649 because of the ongoing wildfires.
- 650 • In 2021, the monthly mean spring BB contribution approached a maximum of 36% (May) due
651 to the strong agricultural fires in Siberia. In August 2021, the IBS received an extremely high
652 BB contribution of 90% from the wildfires in Yakutia located 2000 km away.

653 The increasing trends of occurrence, intensity and duration of wildfires, especially at high
654 northern latitudes, greatly reinforce the importance of carbonaceous light absorption measurements
655 in these areas. These measurements offer valuable insights into the radiative properties of Arctic
656 aerosols, which play a significant role in the enhanced radiative forcing, particularly at short UV-
657 VIS wavelengths. This increased radiative forcing can lead to a pronounced warming effect in the
658 Arctic, with the impact being especially strong during the summer months.

659

660 **Data availability.** All modelling data from this study are available for download from [https://atmo-](https://atmo-access.nilu.no/BELY2_MSU.py)
661 [access.nilu.no/BELY2_MSU.py](https://atmo-access.nilu.no/BELY2_MSU.py). FLEXPART version 10.4 model can be downloaded from
662 <https://www.flexpart.eu/downloads>. Black Carbon observations are available upon request from O.
663 B. Popovicheva.

664

665 **Supplement.** The supplement related to this article is available online at.



666

667 **Author contributions.** OBP supervised the station operation, interpreted data and wrote the
668 manuscript. NE performed all the FLEXPART simulations and analyses, wrote and coordinated the
669 paper. MAC analysed the data, prepared the figures and assisted in the interpretation of the results.
670 ED provided supported AAE calculations and evaluation of data quality. NSK supported the research.
671 All authors contributed to the final version of the manuscript.

672

673 **Competing interests.** The authors declare no competing interests.

674

675 **Acknowledgements.** This research was performed in the frame of the development program of the
676 Interdisciplinary Scientific and Educational School of M. V. Lomonosov Moscow State University
677 “Future Planet and Global Environmental Change”. Authors thank Magee Scientific for AE33
678 instrumentation support and Dr. Asta Gregorič for data examination. V.O. Kobelev is acknowledged
679 data analyses over all study years.

680

681 **Financial support.** The article processing charges for this publication were paid by NILU.
682 Development of the methodology for aethalometric measurements and data treatment was performed
683 in the frame of the RSF project #22-17-00102. Institute of Environmental Survey, Planning and
684 Assessment (IESPA) partly supported the instrumentation and power supply of IBS.

685

686 **References**

- 687 AMAP: AMAP assessment 2015: Black carbon and ozone as Arctic climate forcers, Arctic
688 Monitoring and Assessment Programme (AMAP), Oslo, Norway, 128 pp. pp., 2015.
- 689 AMAP: AMAP Arctic Climate Change Update 2021: Key Trends and Impacts,
690 <https://www.amap.no/documents/download/6759/inline>, 2021.
- 691 Arnold, S. R., Law, K. S., Brock, C. A., Thomas, J. L., Starkweather, S. M., Von Salzen, K., Stohl,
692 A., Sharma, S., Lund, M. T., Flanner, M. G., Petäjä, T., Tanimoto, H., Gamble, J., Dibb, J. E.,
693 Melamed, M., Johnson, N., Fidel, M., Tynkkynen, V. P., Baklanov, A., Eckhardt, S., Monks, S. A.,
694 Browse, J., and Bozem, H.: Arctic air pollution: Challenges and opportunities for the next decade,
695 *Elementa*, 2016, 1–17, <https://doi.org/10.12952/journal.elementa.000104>, 2016.
- 696 Asmi, E., Kivekäs, N., Kerminen, V. M., Komppula, M., Hyvärinen, A. P., Hatakka, J., Viisanen,
697 Y., and Lihavainen, H.: Secondary new particle formation in Northern Finland Pallas site between
698 the years 2000 and 2010, *Atmos. Chem. Phys.*, 11, 12959–12972, [https://doi.org/10.5194/acp-11-](https://doi.org/10.5194/acp-11-12959-2011)
699 12959-2011, 2011.



700 Asmi, E., Backman, J., Servomaa, H., Virkkula, A., Gini, M. I., Eleftheriadis, K., Müller, T., Ohata,
701 S., Kondo, Y., and Hyvärinen, A.: Absorption instruments inter-comparison campaign at the Arctic
702 Pallas station, *Atmos. Meas. Tech.*, 14, 5397–5413, <https://doi.org/10.5194/amt-14-5397-2021>,
703 2021.

704 Backman, J., Schmeisser, L., Virkkula, A., Ogren, J. A., Asmi, E., Starkweather, S., Sharma, S.,
705 Eleftheriadis, K., Uttal, T., Jefferson, A., Bergin, M., Makshtas, A., Tunved, P., and Fiebig, M.: On
706 Aethalometer measurement uncertainties and an instrument correction factor for the Arctic, *Atmos.*
707 *Meas. Tech.*, 10, 5039–5062, <https://doi.org/10.5194/amt-10-5039-2017>, 2017.

708 Bali, K., Banerji, S., Campbell, J. R., Bhakta, A. V., Chen, L. W. A., Holmes, C. D., and Mao, J.:
709 Measurements of brown carbon and its optical properties from boreal forest fires in Alaska summer,
710 *Atmos. Environ.*, 324, 120436, <https://doi.org/10.1016/j.atmosenv.2024.120436>, 2024.

711 Bond, T. C., Doherty, S. J., Fahey, D. W., Forster, P. M., Berntsen, T., Deangelo, B. J., Flanner, M.
712 G., Ghan, S., Kärcher, B., Koch, D., Kinne, S., Kondo, Y., Quinn, P. K., Sarofim, M. C., Schultz,
713 M. G., Schulz, M., Venkataraman, C., Zhang, H., Zhang, S., Bellouin, N., Guttikunda, S. K.,
714 Hopke, P. K., Jacobson, M. Z., Kaiser, J. W., Klimont, Z., Lohmann, U., Schwarz, J. P., Shindell,
715 D., Storelvmo, T., Warren, S. G., and Zender, C. S.: Bounding the role of black carbon in the
716 climate system: A scientific assessment, *J. Geophys. Res. Atmos.*, 118, 5380–5552,
717 <https://doi.org/10.1002/jgrd.50171>, 2013.

718 Bondur, V. G., Voronova, O. S., Cherepanova, E. V., Tsidilina, M. N., and Zima, A. L.:
719 Spatiotemporal Analysis of Multi-Year Wildfires and Emissions of Trace Gases and Aerosols in
720 Russia Based on Satellite Data, *Izv. - Atmos. Ocean Phys.*, 56, 1457–1469,
721 <https://doi.org/10.1134/S0001433820120348>, 2020.

722 Böttcher, K., Paunu, V.-V., Kupiainen, K., Zhizhin, M., Matveev, A., Savolahti, M., Klimont, Z.,
723 Väättäin, S., Lamberg, H., and Karvosenoja, N.: Black carbon emissions from flaring in Russia in
724 the period 2012-2017, *Atmos. Environ.*, 254, 118390,
725 <https://doi.org/10.1016/j.atmosenv.2021.118390>, 2021.

726 Bozem, H., Hoor, P., Kunkel, D., Köllner, F., Schneider, J., Herber, A., Schulz, H., Richard
727 Leaitch, W., Aliabadi, A. A., Willis, M. D., Burkart, J., and Abbatt, J. P. D.: Characterization of
728 transport regimes and the polar dome during Arctic spring and summer using in situ aircraft
729 measurements, *Atmos. Chem. Phys.*, 19, 15049–15071, <https://doi.org/10.5194/acp-19-15049-2019>,
730 2019.

731 Cappa, C. D., Kolesar, K. R., Zhang, X., Atkinson, D. B., Pekour, M. S., Zaveri, R. A., Zelenyuk,
732 A., and Zhang, Q.: Understanding the optical properties of ambient sub-and supermicron particulate
733 matter: Results from the CARES 2010 field study in northern California, *Atmos. Chem. Phys.*, 16,
734 6511–6535, <https://doi.org/10.5194/acp-16-6511-2016>, 2016.



- 735 Cassiani, M., Stohl, A., and Brioude, J.: Lagrangian Stochastic Modelling of Dispersion in the
736 Convective Boundary Layer with Skewed Turbulence Conditions and a Vertical Density Gradient:
737 Formulation and Implementation in the FLEXPART Model, *Boundary-Layer Meteorol.*, 154, 367–
738 390, <https://doi.org/10.1007/s10546-014-9976-5>, 2015.
- 739 Chakrabarty, R. K., Moosmüller, H., Chen, L. W. A., Lewis, K., Arnott, W. P., Mazzoleni, C.,
740 Dubey, M. K., Wold, C. E., Hao, W. M., and Kreidenweis, S. M.: Brown carbon in tar balls from
741 smoldering biomass combustion, *Atmos. Chem. Phys.*, 10, 6363–6370, [https://doi.org/10.5194/acp-](https://doi.org/10.5194/acp-10-6363-2010)
742 10-6363-2010, 2010.
- 743 Chen, X., Kang, S., Yang, J., and Hu, Y.: Contributions of biomass burning in 2019 and 2020 to
744 Arctic black carbon and its transport pathways, *Atmos. Res.*, 296, 107069,
745 <https://doi.org/10.1016/j.atmosres.2023.107069>, 2023.
- 746 Cuesta-Mosquera, A., Glojek, K., Močnik, G., Drinovec, L., Gregorič, A., Rigler, M., Ogrin, M.,
747 Romshoo, B., Weinhold, K., Merkel, M., Van Pinxteren, D., Herrmann, H., Wiedensohler, A.,
748 Pöhlker, M., and Müller, T.: Optical properties and simple forcing efficiency of the organic aerosols
749 and black carbon emitted by residential wood burning in rural central Europe, *Atmos. Chem. Phys.*,
750 24, 2583–2605, <https://doi.org/10.5194/acp-24-2583-2024>, 2024.
- 751 Drinovec, L., Močnik, G., Zotter, P., Prévôt, A. S. H., Ruckstuhl, C., Coz, E., Rupakheti, M.,
752 Sciare, J., Müller, T., Wiedensohler, A., and Hansen, A. D. A.: The “dual-spot” Aethalometer: An
753 improved measurement of aerosol black carbon with real-time loading compensation, *Atmos. Meas.*
754 *Tech.*, 8, 1965–1979, <https://doi.org/10.5194/amt-8-1965-2015>, 2015.
- 755 Eleftheriadis, K., Vratolis, S., and Nyeki, S.: Aerosol black carbon in the European Arctic:
756 Measurements at Zeppelin station, Ny-Ålesund, Svalbard from 1998-2007, *Geophys. Res. Lett.*, 36,
757 1–5, <https://doi.org/10.1029/2008GL035741>, 2009.
- 758 Evangeliou, N., Balkanski, Y., Hao, W. M., Petkov, A., Silverstein, R. P., Corley, R., Nordgren, B.
759 L., Urbanski, S. P., Eckhardt, S., Stohl, A., Tunved, P., Crepinsek, S., Jefferson, A., Sharma, S.,
760 Nøjgaard, J. K., and Skov, H.: Wildfires in northern Eurasia affect the budget of black carbon in the
761 Arctic—a 12-year retrospective synopsis (2002-2013), *Atmos. Chem. Phys.*, 16,
762 <https://doi.org/10.5194/acp-16-7587-2016>, 2016.
- 763 Evangeliou, N., Platt, S., Eckhardt, S., Lund Myhre, C., Laj, P., Alados-Arboledas, L., Backman, J.,
764 Brem, B., Fiebig, M., Flentje, H., Marinoni, A., Pandolfi, M., Yus-Diez, J., Prats, N., Putaud, J.,
765 Sellegri, K., Sorribas, M., Eleftheriadis, K., Vratolis, S., Wiedensohler, A., and Stohl, A.: Changes
766 in black carbon emissions over Europe due to COVID-19 lockdowns, *Atmos. Chem. Phys.*, 1–33,
767 <https://doi.org/10.5194/acp-2020-1005>, 2020.
- 768 Flanner, M. G.: Arctic climate sensitivity to local black carbon, *J. Geophys. Res. Atmos.*, 118,
769 1840–1851, <https://doi.org/10.1002/jgrd.50176>, 2013.



- 770 Forster, C., Stohl, A., and Seibert, P.: Parameterization of convective transport in a Lagrangian
771 particle dispersion model and its evaluation, *J. Appl. Meteorol. Climatol.*, 46, 403–422,
772 <https://doi.org/10.1175/JAM2470.1>, 2007.
- 773 Gilardoni, S., Heslin-Rees, D., Mazzola, M., Vitale, V., Sprenger, M., and Krejci, R.: Drivers
774 controlling black carbon temporal variability in the lower troposphere of the European Arctic,
775 *Atmos. Chem. Phys.*, 23, 15589–15607, <https://doi.org/10.5194/acp-23-15589-2023>, 2023.
- 776 Gramlich, Y., Siegel, K., Haslett, S. L., Cremer, R. S., Lunder, C., Kommula, S. M., Buchholz, A.,
777 Yttri, K. E., Chen, G., Krejci, R., Zieger, P., Virtanen, A., Riipinen, I., and Mohr, C.: Impact of
778 Biomass Burning on Arctic Aerosol Composition,
779 <https://doi.org/10.1021/acsearthspacechem.3c00187>, 2024.
- 780 Grange, S. K., Lötscher, H., Fischer, A., Emmenegger, L., and Hueglin, C.: Evaluation of
781 equivalent black carbon source apportionment using observations from Switzerland between 2008
782 and 2018, *Atmos. Meas. Tech.*, 13, 1867–1885, <https://doi.org/10.5194/amt-13-1867-2020>, 2020.
- 783 Grythe, H., Kristiansen, N. I., Groot Zwaaftink, C. D., Eckhardt, S., Ström, J., Tunved, P., Krejci,
784 R., and Stohl, A.: A new aerosol wet removal scheme for the Lagrangian particle model
785 FLEXPARTv10, *Geosci. Model Dev.*, 10, 1447–1466, <https://doi.org/10.5194/gmd-10-1447-2017>,
786 2017.
- 787 Helin, A., Virkkula, A., Backman, J., Pirjola, L., Sippula, O., Aakko-Saksa, P., Väätäinen, S.,
788 Mylläri, F., Järvinen, A., Bloss, M., Aurela, M., Jakobi, G., Karjalainen, P., Zimmermann, R.,
789 Jokiniemi, J., Saarikoski, S., Tissari, J., Rönkkö, T., Niemi, J. V., and Timonen, H.: Variation of
790 Absorption Ångström Exponent in Aerosols From Different Emission Sources, *J. Geophys. Res.*
791 *Atmos.*, 126, 1–21, <https://doi.org/10.1029/2020JD034094>, 2021.
- 792 Hersbach, H., Bell, B., Berrisford, P., Hirahara, S., Horányi, A., Muñoz-Sabater, J., Nicolas, J.,
793 Peubey, C., Radu, R., Schepers, D., Simmons, A., Soci, C., Abdalla, S., Abellan, X., Balsamo, G.,
794 Bechtold, P., Biavati, G., Bidlot, J., Bonavita, M., De Chiara, G., Dahlgren, P., Dee, D.,
795 Diamantakis, M., Dragani, R., Flemming, J., Forbes, R., Fuentes, M., Geer, A., Haimberger, L.,
796 Healy, S., Hogan, R. J., Hólm, E., Janisková, M., Keeley, S., Laloyaux, P., Lopez, P., Lupu, C.,
797 Radnoti, G., de Rosnay, P., Rozum, I., Vamborg, F., Villaume, S., and Thépaut, J. N.: The ERA5
798 global reanalysis, *Q. J. R. Meteorol. Soc.*, 146, 1999–2049, <https://doi.org/10.1002/qj.3803>, 2020.
- 799 Heslin-Rees, D., Burgos, M., Hansson, H. C., Krejci, R., Ström, J., Tunved, P., and Zieger, P.: From
800 a polar to a marine environment: Has the changing Arctic led to a shift in aerosol light scattering
801 properties?, *Atmos. Chem. Phys.*, 20, 13671–13686, <https://doi.org/10.5194/acp-20-13671-2020>,
802 2020.
- 803 Huang, K., Fu, J. S., Prikhodko, V. Y., Storey, J. M., Romanov, A., Hodson, E. L., Cresko, J.,
804 Morozova, I., Ignatieva, Y., and Cabaniss, J.: Russian anthropogenic black carbon: Emission



- 805 reconstruction and Arctic black carbon simulation, *J. Geophys. Res. Atmos.*, 120, 11306–11333,
806 <https://doi.org/10.1002/2015JD023358>, 2015.
- 807 Ivančič, M., Gregorič, A., Lavrič, G., Alföldy, B., Ježek, I., Hasheminassab, S., Pakbin, P.,
808 Ahangar, F., Sowlat, M., Boddeker, S., and Rigler, M.: Two-year-long high-time-resolution
809 apportionment of primary and secondary carbonaceous aerosols in the Los Angeles Basin using an
810 advanced total carbon–black carbon (TC-BC(λ)) method, *Sci. Total Environ.*, 848,
811 <https://doi.org/10.1016/j.scitotenv.2022.157606>, 2022.
- 812 Johnson, M. S., Strawbridge, K., Knowland, K. E., Keller, C., and Travis, M.: Long-range transport
813 of Siberian biomass burning emissions to North America during FIREX-AQ, *Atmos. Environ.*, 252,
814 118241, <https://doi.org/10.1016/j.atmosenv.2021.118241>, 2021.
- 815 Kaiser, J. W., Heil, A., Andreae, M. O., Benedetti, A., Chubarova, N., Jones, L., Morcrette, J. J.,
816 Razingzer, M., Schultz, M. G., Suttie, M., and Van Der Werf, G. R.: Biomass burning emissions
817 estimated with a global fire assimilation system based on observed fire radiative power,
818 *Biogeosciences*, 9, 527–554, <https://doi.org/10.5194/bg-9-527-2012>, 2012.
- 819 Kanaya, Y., Komazaki, Y., Pochanart, P., Liu, Y., Akimoto, H., Gao, J., Wang, T., and Wang, Z.:
820 Mass concentrations of black carbon measured by four instruments in the middle of Central East
821 China in June 2006, *Atmos. Chem. Phys.*, 8, 7637–7649, <https://doi.org/10.5194/acp-8-7637-2008>,
822 2008.
- 823 Kasischke, E. S. and Turetsky, M. R.: Recent changes in the fire regime across the North American
824 boreal region - Spatial and temporal patterns of burning across Canada and Alaska, *Geophys. Res.*
825 *Let.*, 33, <https://doi.org/10.1029/2006GL025677>, 2006.
- 826 Kharuk, V. I. and Ponomarev, E. I.: Spatiotemporal characteristics of wildfire frequency and
827 relative area burned in larch-dominated forests of Central Siberia, *Russ. J. Ecol.*, 48, 507–512,
828 <https://doi.org/10.1134/S1067413617060042>, 2017.
- 829 Klimont, Z., Kupiainen, K., Heyes, C., Purohit, P., Cofala, J., Rafaj, P., Borken-Kleefeld, J., and
830 Schöpp, W.: Global anthropogenic emissions of particulate matter including black carbon, *Atmos.*
831 *Chem. Phys.*, 17, 8681–8723, <https://doi.org/10.5194/acp-17-508681-2017>, 2017.
- 832 Kostykin, S., Revokatova, A., Chernenkov, A., Ginzburg, V., Polumieva, P., and Zelenova, M.:
833 Black carbon emissions from the siberian fires 2019: Modelling of the atmospheric transport and
834 possible impact on the radiation balance in the arctic region, *Atmosphere (Basel)*, 12,
835 <https://doi.org/10.3390/atmos12070814>, 2021.
- 836 Law, K. S. and Stohl, A.: Arctic Air Pollution: Origins and Impacts, *Science (80-.)*, 315, 1537–
837 1540, <https://doi.org/10.1126/science.1137695>, 2007.
- 838 Lee, Y. H., Lamarque, J. F., Flanner, M. G., Jiao, C., Shindell, D. T., Berntsen, T., Bisiaux, M. M.,
839 Cao, J., Collins, W. J., Curran, M., Edwards, R., Faluvegi, G., Ghan, S., Horowitz, L., McConnell,



840 J. R., Ming, J., Myhre, G., Nagashima, T., Naik, V., Rumbold, S. T., Skeie, R. B., Sudo, K.,
841 Takemura, T., Thevenon, F., Xu, B., and Yoon, J. H.: Evaluation of preindustrial to present-day
842 black carbon and its albedo forcing from Atmospheric Chemistry and Climate Model
843 Intercomparison Project (ACCMIP), *Atmos. Chem. Phys.*, 13, 2607–2634,
844 <https://doi.org/10.5194/acp-13-2607-2013>, 2013.

845 Manousakas, M., Popovicheva, O., Evangelidou, N., Diapouli, E., Sitnikov, N., Shonija, N., and
846 Eleftheriadis, K.: Aerosol carbonaceous, elemental and ionic composition variability and origin at
847 the Siberian High Arctic, Cape Baranova, *Tellus B Chem. Phys. Meteorol.*, 72, 1–14,
848 <https://doi.org/10.1080/16000889.2020.1803708>, 2020.

849 Markowicz, K. M., Pakszys, P., Ritter, C., Zielinski, T., Udisti, R., Cappelletti, D., Mazzola, M.,
850 Shiobara, M., Xian, P., Zawadzka, O., Lisok, J., Petelski, T., Makuch, P., and Karasinski, G.:
851 Impact of North American intense fires on aerosol optical properties measured over the European
852 Arctic in July 2015, *J. Geophys. Res.*, 121, 14487–14512, <https://doi.org/10.1002/2016JD025310>,
853 2016.

854 Massling, A., Nielsen, I. E., Kristensen, D., Christensen, J. H., Sorensen, L. L., Jensen, B., Nguyen,
855 Q. T., Nøjgaard, J. K., Glasius, M., and Skov, H.: Atmospheric black carbon and sulfate
856 concentrations in Northeast Greenland, *Atmos. Chem. Phys.*, 15, 9681–9692,
857 <https://doi.org/10.5194/acp-15-9681-2015>, 2015.

858 Mokhov, I. I., Bondur, V. G., Sitnov, S. A., and Voronova, O. S.: Satellite Monitoring of Wildfires
859 and Emissions into the Atmosphere of Combustion Products in Russia: Relation to Atmospheric
860 Blockings, *Dokl. Earth Sci.*, 495, 921–924, <https://doi.org/10.1134/S1028334X20120089>, 2020.

861 Moschos, V., Schmale, J., Aas, W., Becagli, S., Calzolari, G., Eleftheriadis, K., Moffett, C. E.,
862 Schnelle-Kreis, J., Severi, M., Sharma, S., Skov, H., Vestenius, M., Zhang, W., Hakola, H., Hellén,
863 H., Huang, L., Jaffrezo, J. L., Massling, A., Nøjgaard, J. K., Petäjä, T., Popovicheva, O., Sheesley,
864 R. J., Traversi, R., Yttri, K. E., Prévôt, A. S. H., Baltensperger, U., and El Haddad, I.: Elucidating
865 the present-day chemical composition, seasonality and source regions of climate-relevant aerosols
866 across the Arctic land surface, *Environ. Res. Lett.*, 17, <https://doi.org/10.1088/1748-9326/ac444b>,
867 2022a.

868 Moschos, V., Dzepina, K., Bhattu, D., Lamkaddam, H., Casotto, R., Daellenbach, K. R., Canonaco,
869 F., Rai, P., Aas, W., Becagli, S., Calzolari, G., Eleftheriadis, K., Moffett, C. E., Schnelle-Kreis, J.,
870 Severi, M., Sharma, S., Skov, H., Vestenius, M., Zhang, W., Hakola, H., Hellén, H., Huang, L.,
871 Jaffrezo, J. L., Massling, A., Nøjgaard, J. K., Petäjä, T., Popovicheva, O., Sheesley, R. J., Traversi,
872 R., Yttri, K. E., Schmale, J., Prévôt, A. S. H., Baltensperger, U., and El Haddad, I.: Equal
873 abundance of summertime natural and wintertime anthropogenic Arctic organic aerosols, *Nat.*
874 *Geosci.*, 15, 196–202, <https://doi.org/10.1038/s41561-021-00891-1>, 2022b.



- 875 Ohata, S., Mori, T., Kondo, Y., Sharma, S., Hyvärinen, A., Andrews, E., Tunved, P., Asmi, E.,
876 Backman, J., Servomaa, H., Veber, D., Eleftheriadis, K., Vratolis, S., Krejci, R., Zieger, P., Koike,
877 M., Kanaya, Y., Yoshida, A., Moteki, N., Zhao, Y., Tobo, Y., Matsushita, J., and Oshima, N.:
878 Estimates of mass absorption cross sections of black carbon for filter-based absorption photometers
879 in the Arctic, *Atmos. Meas. Tech.*, 14, 6723–6748, <https://doi.org/10.5194/amt-14-6723-2021>,
880 2021.
- 881 Paris, J.-D., Stohl, A., Nédélec, P., Arshinov, M. Y., Panchenko, M. V., Shmargunov, V. P., Law,
882 K. S., Belan, B. D., and Ciais, P.: Wildfire smoke in the Siberian Arctic in summer: source
883 characterization and plume evolution from airborne measurements, *Atmos. Chem. Phys.*, 9, 9315–
884 9327, <https://doi.org/10.5194/acp-9-9315-2009>, 2009, 2009.
- 885 Petzold, A., Rasp, K., Weinzierl, B., Esselborn, M., Hamburger, T., Dörnbrack, A., Kandler, K.,
886 Schütz, L., Knippertz, P., Fiebig, M., and Virkkula, A.: Saharan dust absorption and refractive
887 index from aircraft-based observations during SAMUM 2006, *Tellus, Ser. B Chem. Phys.*
888 *Meteorol.*, 61, 118–130, <https://doi.org/10.1111/j.1600-0889.2008.00383.x>, 2009.
- 889 Petzold, A., Ogren, J. A., Fiebig, M., Laj, P., Li, S. M., Baltensperger, U., Holzer-Popp, T., Kinne,
890 S., Pappalardo, G., Sugimoto, N., Wehrli, C., Wiedensohler, A., and Zhang, X. Y.:
891 Recommendations for reporting black carbon measurements, *Atmos. Chem. Phys.*, 13, 8365–8379,
892 <https://doi.org/10.5194/acp-13-8365-2013>, 2013.
- 893 Pissou, I., Sollum, E., Grythe, H., Kristiansen, N. I., Cassiani, M., Eckhardt, S., Arnold, D., Morton,
894 D., Thompson, R. L., Groot Zwaaftink, C. D., Evangeliou, N., Sodemann, H., Haimberger, L.,
895 Henne, S., Brunner, D., Burkhart, J. F., Fouilloux, A., Brioude, J., Philipp, A., Seibert, P., and
896 Stohl, A.: The Lagrangian particle dispersion model FLEXPART version 10.4, *Geosci. Model Dev.*,
897 12, 4955–4997, <https://doi.org/10.5194/gmd-12-4955-2019>, 2019.
- 898 Platt, S., Hov, Ø., Berg, T., Breivik, K., Eckhardt, S., Eleftheriadis, K., Evangeliou, N., Fiebig, M.,
899 Fisher, R., Hansen, G., Hansson, H.-C., Heintzenberg, J., Hermansen, O., Heslin-Rees, D., Holmén,
900 K., Hudson, S., Kallenborn, R., Krejci, R., Krognnes, T., Larssen, S., Lowry, D., Lund Myhre, C.,
901 Lunder, C., Nisbet, E., Nizetto, P., Park, K.-T., Pedersen, C., Aspö Pfaffhuber, K., Röckmann, T.,
902 Schmidbauer, N., Solberg, S., Stohl, A., Ström, J., Svendby, T., Tunved, P., Tørnkvist, K., van der
903 Veen, C., Vratolis, S., Yoon, Y. J., Yttri, K. E., Zieger, P., Aas, W., and Tørseth, K.: Atmospheric
904 composition in the European Arctic and 30 years of the Zeppelin Observatory, Ny-Ålesund, *Atmos.*
905 *Chem. Phys.*, 1–80, 2021.
- 906 Popovicheva, O., Diapouli, E., Makshatas, A., Shonija, N., Manousakas, M., Saraga, D., Uttal, T.,
907 and Eleftheriadis, K.: East Siberian Arctic background and black carbon polluted aerosols at HMO
908 Tiksi, *Sci. Total Environ.*, 655, 924–938, <https://doi.org/10.1016/j.scitotenv.2018.11.165>, 2019a.
- 909 Popovicheva, O. B., Shonija, N. K., Persiantseva, N., Timofeev, M., Diapouli, E., Eleftheriadis, K.,



- 910 Borgese, L., and Nguyen, X. A.: Aerosol pollutants during agricultural biomass burning: A case
911 study in Ba Vi Region in Hanoi, Vietnam, *Aerosol Air Qual. Res.*, 17, 2762–2779,
912 <https://doi.org/10.4209/aaqr.2017.03.0111>, 2017a.
- 913 Popovicheva, O. B., Evangeliou, N., Eleftheriadis, K., Kalogridis, A. C., Sitnikov, N., Eckhardt, S.,
914 and Stohl, A.: Black Carbon Sources Constrained by Observations in the Russian High Arctic,
915 *Environ. Sci. Technol.*, 51, <https://doi.org/10.1021/acs.est.6b05832>, 2017b.
- 916 Popovicheva, O. B., Engling, G., Ku, I. T., Timofeev, M. A., and Shonija, N. K.: Aerosol emissions
917 from long-lasting smoldering of boreal peatlands: Chemical composition, markers, and
918 microstructure, *Aerosol Air Qual. Res.*, 19, 484–503, <https://doi.org/10.4209/aaqr.2018.08.0302>,
919 2019b.
- 920 Popovicheva, O. B., Evangeliou, N., Kobelev, V. O., Chichaeva, M. A., Eleftheriadis, K., Gregorič,
921 A., and Kasimov, N. S.: Siberian Arctic black carbon: gas flaring and wildfire impact, *Atmos.*
922 *Chem. Phys.*, 22, 5983–6000, <https://doi.org/10.5194/acp-22-5983-2022>, 2022.
- 923 Popovicheva, O. B., Chichaeva, M. A., Kobelev, V. O., and Kasimov, N. S.: Black Carbon
924 Seasonal Trends and Regional Sources on Bely Island (Arctic), *Atmos. Ocean. Opt.*, 36, 176–184,
925 <https://doi.org/10.1134/S1024856023030090>, 2023.
- 926 Pulimeno, S., Bruschi, F., Feltracco, M., Mazzola, M., Gilardoni, S., Crocchianti, S., Cappelletti,
927 D., Gambaro, A., and Barbaro, E.: Investigating the Presence of Biomass Burning Events at Ny-Å
928 Lesund: Optical and Chemical Insights from Summer-Fall 2019, *Atmos. Environ.*, 320, 120336,
929 <https://doi.org/10.1016/j.atmosenv.2024.120336>, 2024.
- 930 Qi, L. and Wang, S.: Sources of black carbon in the atmosphere and in snow in the Arctic, *Sci.*
931 *Total Environ.*, 691, 442–454, <https://doi.org/10.1016/j.scitotenv.2019.07.073>, 2019.
- 932 Ran, L., Deng, Z. Z., Wang, P. C., and Xia, X. A.: Black carbon and wavelength-dependent aerosol
933 absorption in the North China Plain based on two-year aethalometer measurements, *Atmos.*
934 *Environ.*, 142, 132–144, <https://doi.org/10.1016/j.atmosenv.2016.07.014>, 2016.
- 935 Rogers, B. M., Balch, J. K., Goetz, S. J., Lehmann, C. E. R., and Turetsky, M.: Focus on changing
936 fire regimes: interactions with climate, ecosystems, and society, *Environ. Res. Lett.*, 15,
937 <https://doi.org/10.1088/1748-9326/ab6d3a>, 2020.
- 938 Sandradewi, J., Prévôt, A. S. H., Szidat, S., Perron, N., Alfarra, M. R., Lanz, V. A., Weingartner,
939 E., and Baltensperger, U. R. S.: Using aerosol light absorption measurements for the quantitative
940 determination of wood burning and traffic emission contribution to particulate matter, *Environ. Sci.*
941 *Technol.*, 42, 3316–3323, <https://doi.org/10.1021/es702253m>, 2008.
- 942 Schmale, J., Zieger, P., and Ekman, A. M. L.: Aerosols in current and future Arctic climate, *Nat.*
943 *Clim. Chang.*, 11, 95–105, <https://doi.org/10.1038/s41558-020-00969-5>, 2021.
- 944 Schmale, J., Sharma, S., Decesari, S., Pernov, J., Massling, A., Hansson, H. C., Von Salzen, K.,



- 945 Skov, H., Andrews, E., Quinn, P. K., Upchurch, L. M., Eleftheriadis, K., Traversi, R., Gilardoni, S.,
946 Mazzola, M., Laing, J., and Hopke, P.: Pan-Arctic seasonal cycles and long-term trends of aerosol
947 properties from 10 observatories, *Atmos. Chem. Phys.*, 22, 3067–3096, [https://doi.org/10.5194/acp-](https://doi.org/10.5194/acp-22-3067-2022)
948 [22-3067-2022](https://doi.org/10.5194/acp-22-3067-2022), 2022.
- 949 Schmeisser, L., Backman, J., Ogren, J. A., Andrews, E., Asmi, E., Starkweather, S., Uttal, T.,
950 Fiebig, M., Sharma, S., Eleftheriadis, K., Vratolis, S., Bergin, M., Tunved, P., and Jefferson, A.:
951 Seasonality of aerosol optical properties in the Arctic, *Atmos. Chem. Phys.*, 18, 11599–11622,
952 <https://doi.org/10.5194/acp-18-11599-2018>, 2018.
- 953 Schneider, E., Czech, H., Popovicheva, O., Chichayeva, M., Kobelev, V., Kasimov, N., Minkina, T.,
954 R ger, C. P., and Zimmermann, R.: Mass spectrometric analysis of unprecedented high levels of
955 carbonaceous aerosol particles long-range transported from wildfires in the Siberian Arctic, *Atmos.*
956 *Chem. Phys.*, 24, 553–576, <https://doi.org/10.5194/acp-24-553-2024>, 2024.
- 957 Sharma, S., Lavou , D., Chachier, H., Barrie, L. A., and Gong, S. L.: Long-term trends of the black
958 carbon concentrations in the Canadian Arctic, *J. Geophys. Res. D Atmos.*, 109, 1–10,
959 <https://doi.org/10.1029/2003JD004331>, 2004.
- 960 Sharma, S., Ishizawa, M., Chan, D., Lavou , D., Andrews, E., Eleftheriadis, K., and Maksyutov, S.:
961 16-year simulation of arctic black carbon: Transport, source contribution, and sensitivity analysis on
962 deposition, *J. Geophys. Res. Atmos.*, 118, 943–964, <https://doi.org/10.1029/2012JD017774>, 2013.
- 963 Sharma, S., Richard Leaitch, W., Huang, L., Veber, D., Kolonjari, F., Zhang, W., Hanna, S. J.,
964 Bertram, A. K., and Ogren, J. A.: An evaluation of three methods for measuring black carbon in
965 Alert, Canada, *Atmos. Chem. Phys.*, 17, 15225–15243, <https://doi.org/10.5194/acp-17-15225-2017>,
966 2017.
- 967 Silver, B., Arnold, S. R., Reddington, C. L., Emmons, L. K., and Conibear, L.: Large transboundary
968 health impact of Arctic wildfire smoke, *Commun. Earth Environ.*, 5,
969 <https://doi.org/10.1038/s43247-024-01361-3>, 2024.
- 970 Singh, M., Kondo, Y., Ohata, S., Mori, T., Oshima, N., Hyv rinen, A., Backman, J., Asmi, E.,
971 Servomaa, H., Schnaiter, F. M., Andrews, E., Sharma, S., Eleftheriadis, K., Vratolis, S., Zhao, Y.,
972 Koike, M., Moteki, N., and Sinha, P. R.: Mass absorption cross section of black carbon for
973 Aethalometer in the Arctic, *Aerosol Sci. Technol.*, 58, 536–553,
974 <https://doi.org/10.1080/02786826.2024.2316173>, 2024.
- 975 Stathopoulos, V. K., Evangelidou, N., Stohl, A., Vratolis, S., Matsoukas, C., and Eleftheriadis, K.:
976 Large Circulation Patterns Strongly Modulate Long-Term Variability of Arctic Black Carbon
977 Levels and Areas of Origin, *Geophys. Res. Lett.*, 48, 1–10, <https://doi.org/10.1029/2021GL092876>,
978 2021.
- 979 Stohl, A.: Characteristics of atmospheric transport into the Arctic troposphere, *J. Geophys. Res.*



- 980 Atmos., 111, 1–17, <https://doi.org/10.1029/2005JD006888>, 2006.
- 981 Stohl, A., Forster, C., Frank, A., Seibert, P., and Wotawa, G.: Technical note: The Lagrangian
982 particle dispersion model FLEXPART version 6.2, Atmos. Chem. Phys., 5, 2461–2474,
983 <https://doi.org/10.5194/acp-5-2461-2005>, 2005.
- 984 Stohl, A., Klimont, Z., Eckhardt, S., Kupiainen, K., Shevchenko, V. P., Kopeikin, V. M., and
985 Novigatsky, A. N.: Black carbon in the Arctic: The underestimated role of gas flaring and
986 residential combustion emissions, Atmos. Chem. Phys., 13, 8833–8855,
987 <https://doi.org/10.5194/acp-13-8833-2013>, 2013.
- 988 Stone, R. S., Sharma, S., Herber, A., Eleftheriadis, K., and Nelson, D. W.: A characterization of
989 Arctic aerosols on the basis of aerosol optical depth and black carbon measurements, Elem. Sci.
990 Anthr., 2, 1–22, <https://doi.org/10.12952/journal.elementa.000027>, 2014.
- 991 Therneau, T.: deming: Deming, Theil-Sen, Passing-Bablok and Total Least Squares Regression,
992 2024.
- 993 Tomshin, O. and Solovyev, V.: Features of the Extreme Fire Season of 2021 in Yakutia (Eastern
994 Siberia) and Heavy Air Pollution Caused by Biomass Burning, Remote Sens., 14,
995 <https://doi.org/10.3390/rs14194980>, 2022.
- 996 Tunved, P., Ström, J., and Krejci, R.: Arctic aerosol life cycle: Linking aerosol size distributions
997 observed between 2000 and 2010 with air mass transport and precipitation at Zeppelin station, Ny-
998 Ålesund, Svalbard, Atmos. Chem. Phys., 13, 3643–3660, [https://doi.org/10.5194/acp-13-3643-](https://doi.org/10.5194/acp-13-3643-2013)
999 2013, 2013.
- 1000 Ulevicius, V., Byčenkienė, S., Remeikis, V., Garbaras, A., Kecorius, S., Andriejauskienė, J.,
1001 Jasinevičienė, D., and Mocnik, G.: Characterization of pollution events in the East Baltic region
1002 affected by regional biomass fire emissions, Atmos. Res., 98, 190–200,
1003 <https://doi.org/10.1016/j.atmosres.2010.03.021>, 2010.
- 1004 Veraverbeke, S., Rogers, B. M., Goulden, M. L., Jandt, R. R., Miller, C. E., Wiggins, E. B., and
1005 Randerson, J. T.: Lightning as a major driver of recent large fire years in North American boreal
1006 forests, Nat. Clim. Chang., 7, 529–534, <https://doi.org/10.1038/nclimate3329>, 2017.
- 1007 Vinogradova, A. A. and Ivanova, Y. A.: Atmospheric Transport of Black Carbon to the Russian
1008 Arctic from Different Sources: Winter and Summer 2000–2016, Atmos. Ocean. Opt., 36, 758–766,
1009 <https://doi.org/10.1134/S1024856023060222>, 2023.
- 1010 Virkkula, A.: Modeled source apportionment of black carbon particles coated with a light-scattering
1011 shell, Atmos. Meas. Tech., 14, 3707–3719, <https://doi.org/10.5194/amt-14-3707-2021>, 2021.
- 1012 Voronova, O. S., Zima, A. L., Kladov, V. L., and Cherepanova, E. V.: Anomalous Wildfires in
1013 Siberia in Summer 2019, Izv. - Atmos. Ocean Phys., 56, 1042–1052,
1014 <https://doi.org/10.1134/S000143382009025X>, 2020.



- 1015 Voronova, O. S., Gordo, K. A., Zima, A. L., and Feoktistova, N. V.: Strong Wildfires in the
1016 Russian Federation in 2021 Detected Using Satellite Data, *Izv. - Atmos. Ocean Phys.*, 58, 1065–
1017 1076, <https://doi.org/10.1134/S0001433822090225>, 2022.
- 1018 Willis, M. D., Leaitch, W. R., and Abbatt, J. P. D.: Processes Controlling the Composition and
1019 Abundance of Arctic Aerosol, *Rev. Geophys.*, 56, 621–671,
1020 <https://doi.org/10.1029/2018RG000602>, 2018.
- 1021 Winiger, P., Andersson, A., Eckhardt, S., Stohl, A., Semiletov, I. P., Dudarev, O. V., Charkin, A.,
1022 Shakhova, N., Klimont, Z., Heyes, C., and Gustafsson, Ö.: Siberian Arctic black carbon sources
1023 constrained by model and observation, *Proc. Natl. Acad. Sci.*, 114, E1054–E1061,
1024 <https://doi.org/10.1073/pnas.1613401114>, 2017.
- 1025 Winiger, P., Barrett, T. E., Sheesley, R. J., Huang, L., Sharma, S., Barrie, L. A., and Yttri, K. E.:
1026 Source apportionment of circum-Arctic atmospheric black carbon from isotopes and modeling, *Sci.*
1027 *Adv.*, 5, eaau8052, <https://doi.org/10.1126/sciadv.aau8052>, 2019.
- 1028 Yttri, K. E., Lund Myhre, C., Eckhardt, S., Fiebig, M., Dye, C., Hirdman, D., Ström, J., Klimont,
1029 Z., and Stohl, A.: Quantifying black carbon from biomass burning by means of levoglucosan - A
1030 one-year time series at the Arctic observatory Zeppelin, *Atmos. Chem. Phys.*, 14, 6427–6442,
1031 <https://doi.org/10.5194/acp-14-6427-2014>, 2014.
- 1032 Yttri, K. E., Bäcklund, A., Conen, F., Eckhardt, S., Evangeliou, N., Fiebig, M., Kasper-Giebl, A.,
1033 Gold, A., Gundersen, H., Myhre, C. L., Platt, S. M., Simpson, D., Surratt, J. D., Szidat, S., Rauber,
1034 M., Torseth, K., Ytre-Eide, M. A., Zhang, Z., and Aas, W.: Composition and sources of
1035 carbonaceous aerosol in the European Arctic at Zeppelin Observatory, Svalbard, *Atmos. Chem.*
1036 *Phys.*, 24, 2731–2758, 2024.
- 1037 Yue, S., Zhu, J., Chen, S., Xie, Q., Li, W., Li, L., Ren, H., Su, S., Li, P., Ma, H., Fan, Y., Cheng, B.,
1038 Wu, L., Deng, J., Hu, W., Ren, L., Wei, L., Zhao, W., Tian, Y., Pan, X., Sun, Y., Wang, Z., Wu, F.,
1039 Liu, C. Q., Su, H., Penner, J. E., Pöschl, U., Andreae, M. O., Cheng, Y., and Fu, P.: Brown carbon
1040 from biomass burning imposes strong circum-Arctic warming, *One Earth*, 5, 293–304,
1041 <https://doi.org/10.1016/j.oneear.2022.02.006>, 2022.
- 1042 Zanatta, M., Laj, P., Gysel, M., Baltensperger, U., Vratolis, S., Eleftheriadis, K., Kondo, Y.,
1043 Dubuisson, P., Winiarek, V., Kazadzis, S., Tunved, P., and Jacobi, H. W.: Effects of mixing state on
1044 optical and radiative properties of black carbon in the European Arctic, *Atmos. Chem. Phys.*, 18,
1045 14037–14057, <https://doi.org/10.5194/acp-18-14037-2018>, 2018.
- 1046 Zenkova, P. N., Chernov, D. G., Shmargunov, V. P., Panchenko, M. V., and Belan, B. D.:
1047 Submicron Aerosol and Absorbing Substance in the Troposphere of the Russian Sector of the Arctic
1048 According to Measurements Onboard the Tu-134 Optik Aircraft Laboratory in 2020, *Atmos. Ocean.*
1049 *Opt.*, 35, 43–51, <https://doi.org/10.1134/S1024856022010146>, 2022.

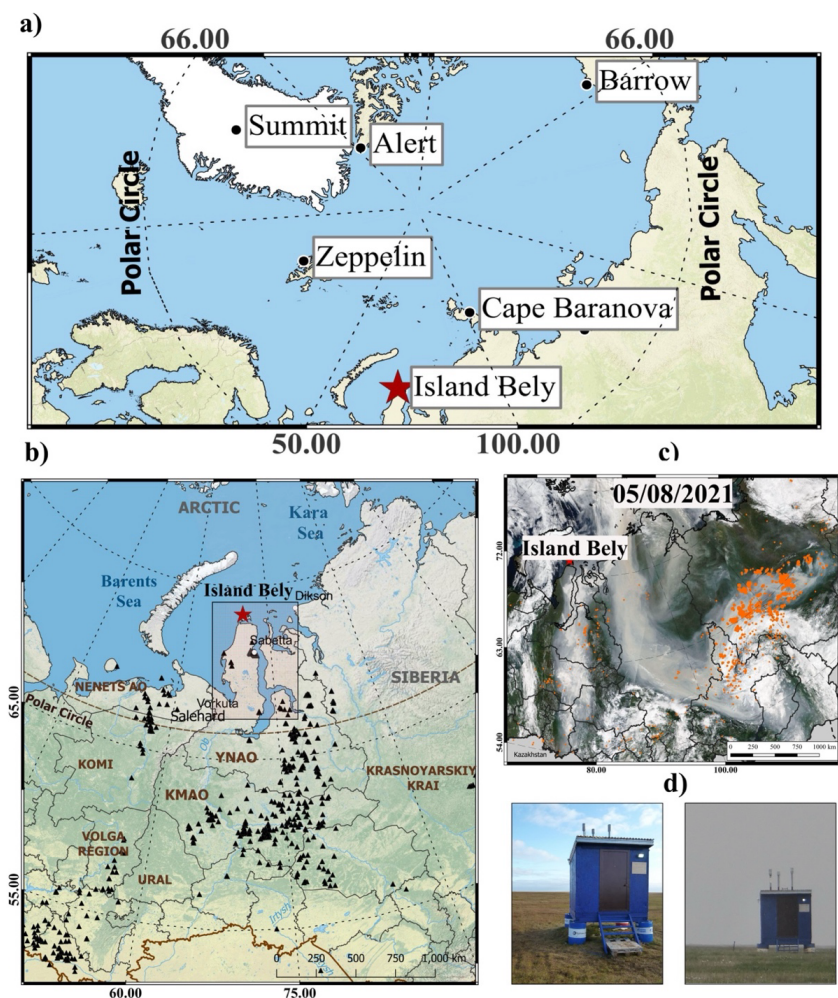


1050 Zhou, C., Penner, J. E., Flanner, M. G., Bisiaux, M. M., Edwards, R., and McConnell, J. R.:
1051 Transport of black carbon to polar regions: Sensitivity and forcing by black carbon, *Geophys. Res.*
1052 *Let.*, 39, 1–6, <https://doi.org/10.1029/2012GL053388>, 2012.
1053 Zhu, C., Kanaya, Y., Takigawa, M., Ikeda, K., Tanimoto, H., Taketani, F., Miyakawa, T.,
1054 Kobayashi, H., and Pissò, I.: FLEXPART v10.1 simulation of source contributions to Arctic black
1055 carbon, *Atmos. Chem. Phys.*, 20, 1641–1656, <https://doi.org/10.5194/acp-20-1641-2020>, 2020.
1056
1057



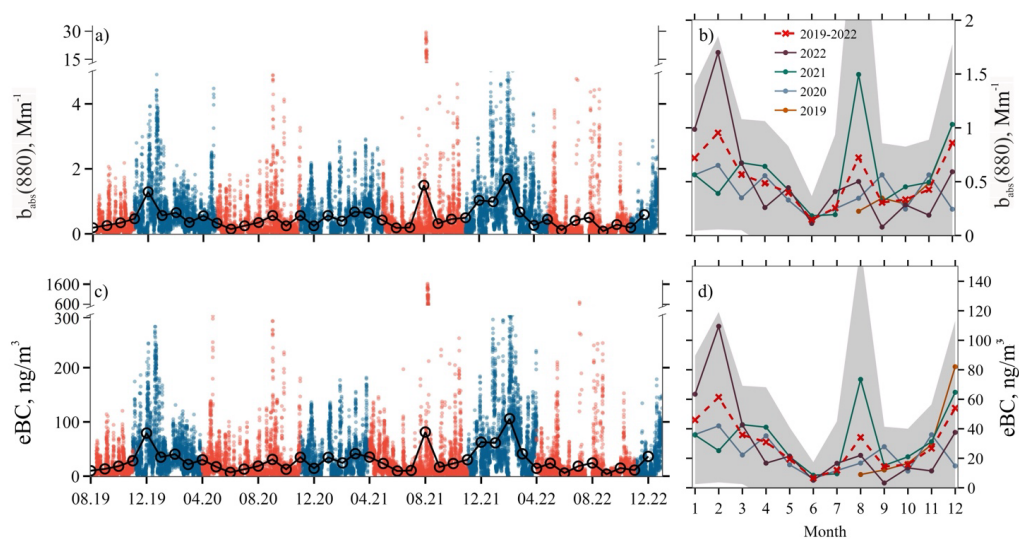
1058 FIGURES & LEGENDS

1059



1060

1061 **Figure 1.** (a) The “Island Bely” station (IBS) between other polar aerosol stations. (b) A map
1062 showing IBS in Western Siberia along with oil and gas fields (adopted from <https://skytruth.org/>,
1063 last access: 7 November 2024). Flares of oil and gas fields are indicated for 2020 as black triangles
1064 (<https://skytruth.org/>, last access: 7 November 2024). (c) Satellite image of strong plume from the
1065 area of Yakutian wildfires which brought deep smoke to the Bely Island. (d) View to the pavilion of
1066 IBS under clear conditions on 25 July 2021, and during the unprecedented smoke event on 5 August
1067 2021. Maps were created using Open-Source Geographic Information System QGIS
1068 (<https://qgis.org/en/site>, last access: 7 November 2024) with ESRI physical imagery
1069 (https://server.arcgisonline.com/ArcGIS/rest/services/World_Physical_Map/MapServer/tile/%7Bz%7D/%7Bx%7D/%7By%7D/%7Bx%7D&zmax=20&zmin=0, last access: 7 November 2024) as the base layer,
1070 and for MODIS Reflectance true color imagery (MODIS Science Team) and Satellite imagery from
1071 05 of August 2021 (<https://worldview.earthdata.nasa.gov>, last access: 7 November 2024) with
1072 TERRA MODIS fire anomaly layer. Open-source Natural Earth quick start (NEQS) package was
1073 used to add layers of natural and cultural boundaries and polygons from ESRI Shapefile storage.
1074

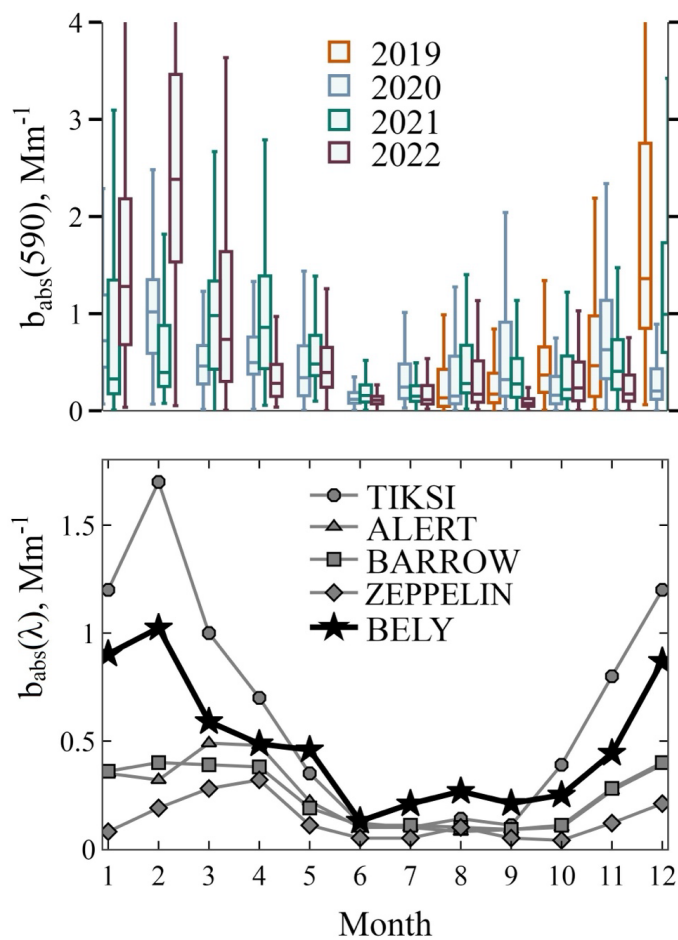


1075

1076 **Figure 2.** Hourly timeseries and monthly means of (a) $b_{abs}(880)$ and (c) eBC for cold (blue) and
1077 warm (red) periods; monthly climatology of (b) $b_{abs}(880)$ and (d) eBC for half year 2019 and 2020,
1078 2021, and 2022. Cross-marks (x) joined by lines show the inter-annual mean; the standard deviation
1079 is plotted by shadow area.

1080

1081

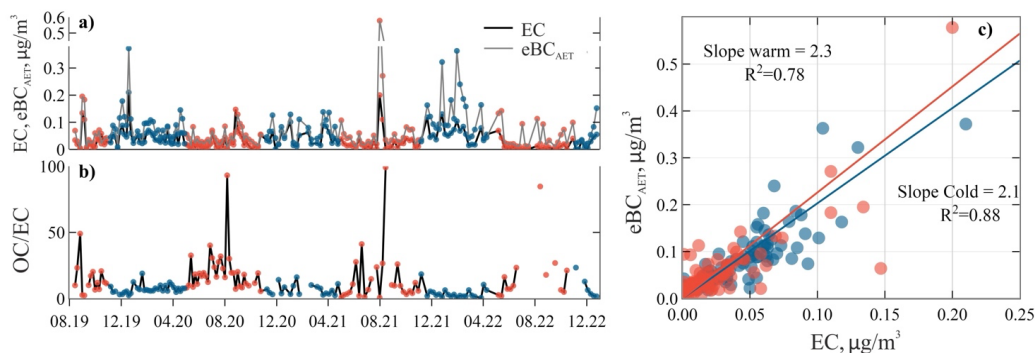


1082

1083 **Figure 3.** (a) Monthly box-whisker plot for $b_{abs}(550)$ at IBS for half year 2019 and full 2020, 2021,
1084 and 2022. The 25th, 50th, and 75th percentiles are shown with boxes, while whiskers extend ± 1.5 times
1085 the interquartile range. (b) Seasonality of monthly median of b_{abs} at 550 nm at Tiksi, Alert, Barrow,
1086 Zepelin for 2012-2014 (Schmeisser et al., 2018), and b_{abs} at 590 nm at IBS for 2019-2022 (this work).

1087

1088

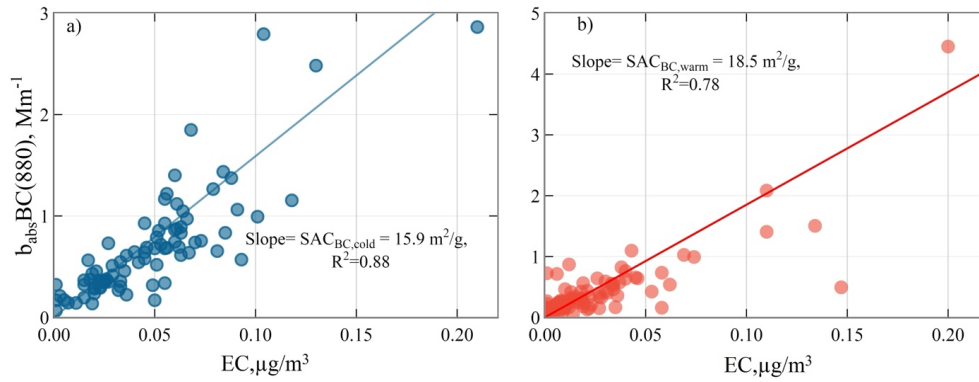


1089

1090 **Figure 4.** Temporal variation of (a) weekly EC and eBC_{AET} averaged over the whole sampling
1091 period and (b) the OC/EC ratio. (c) Scatter plots and orthogonal regressions (solid lines) for
1092 measured eBC_{AET} and EC concentrations in cold (blue) and warm (red) period. The figure includes
1093 the regression slope, the coefficient of determination (R^2).

1094

1095

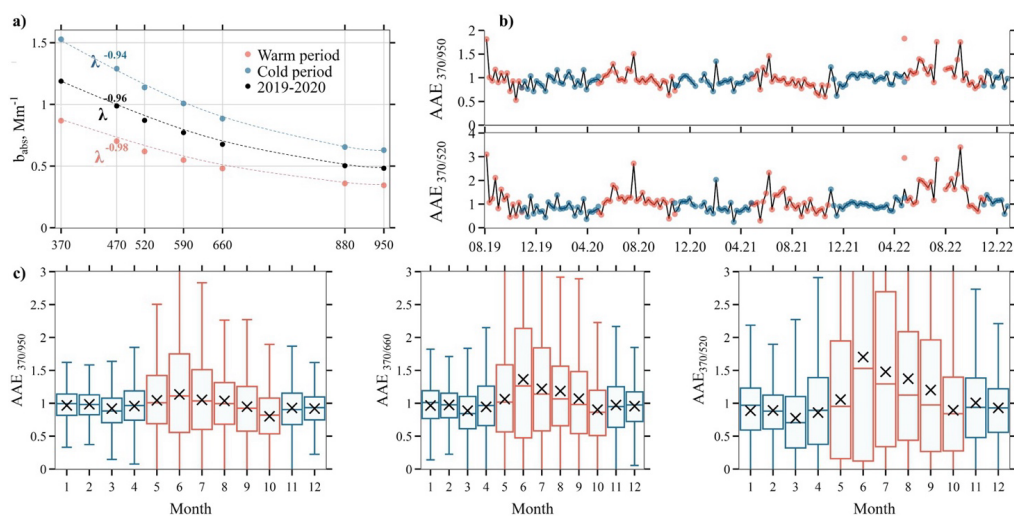


1096

1097 **Figure 5.** Scatter plots and orthogonal regressions (solid line) for $b_{abs}/BC(880)$ and EC
1098 concentrations for the (a) cold (blue) and (b) warm (red) periods. Regression slope defines
1099 $SAC_{BC,cold}$ and $SAC_{BC,warm}$.

1100

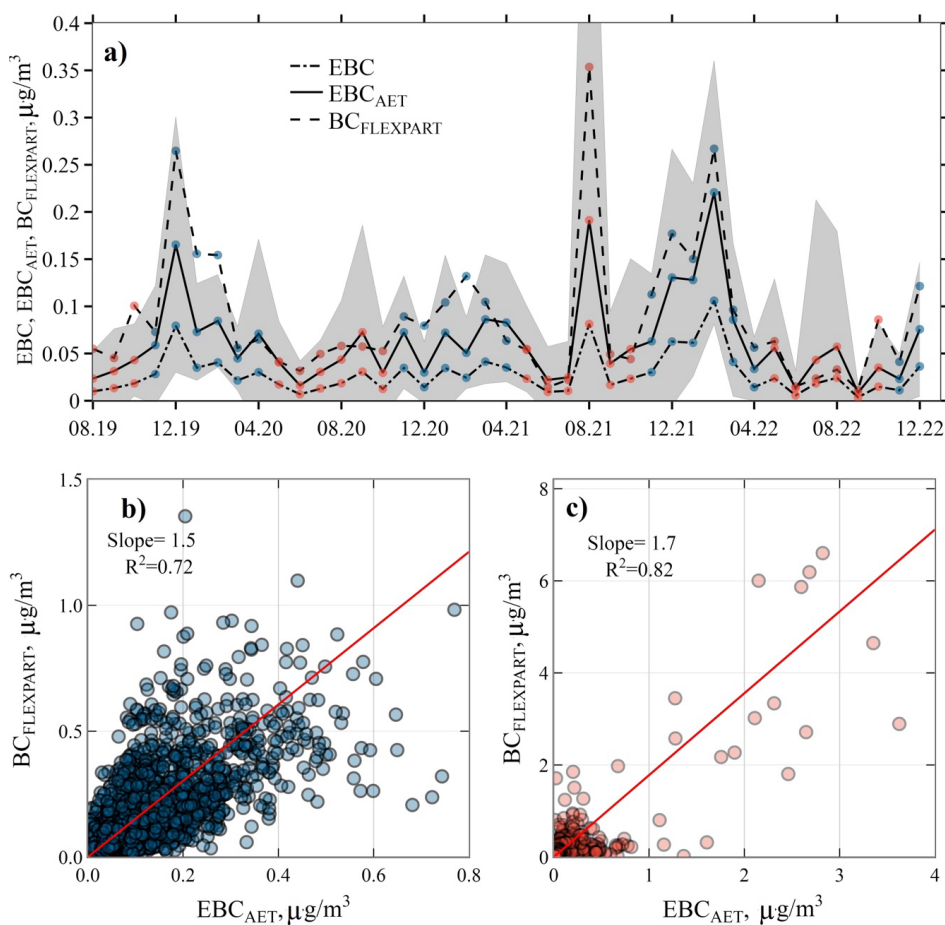
1101



1102

1103 **Figure 6.** (a) Spectral dependence of light absorption coefficient for 2019-2022, during warm (red)
1104 and cold (blue) periods. $AAE_{350/950}$ is the slope of the linear regression in logarithmic scale of a
1105 power law regression, Eq.1. (b) Timeseries of $AAE_{370/950}$ and $AAE_{370/520}$. (c) Box-whisker plots
1106 and monthly means of AAE at 370 and 950 nm, 370 and 660 nm, and 370 and 520 nm for the entire
1107 period.

1108



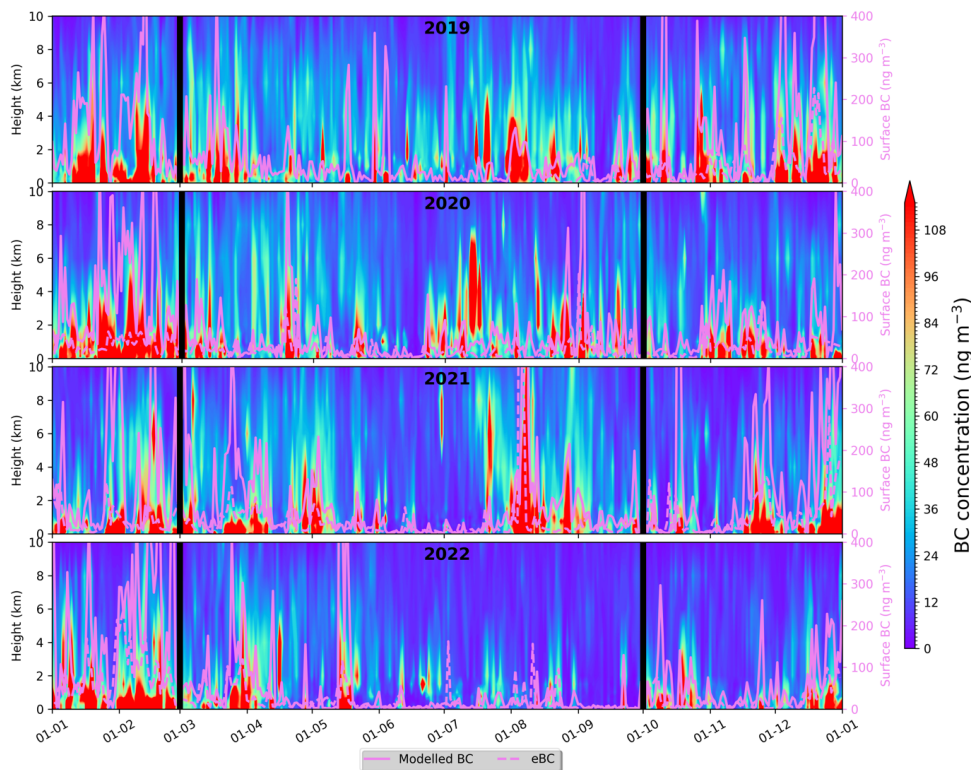
1109

1110 **Figure 7.** (a) Monthly mean eBC and modelled surface BC concentrations from 10 August 2019 to
1111 31 December 2022. Monthly mean eBC_{AET} (line with crosses) shown with the standard deviation
1112 range by shadowed area. Scatter plots and orthogonal regressions (solid lines) for $BC_{FLEXPART}$
1113 calculated over measured eBC_{AET} concentrations for (b) cold and (c) warm period. The figure
1114 includes the regression slope, the coefficient of determination (R^2).

1115



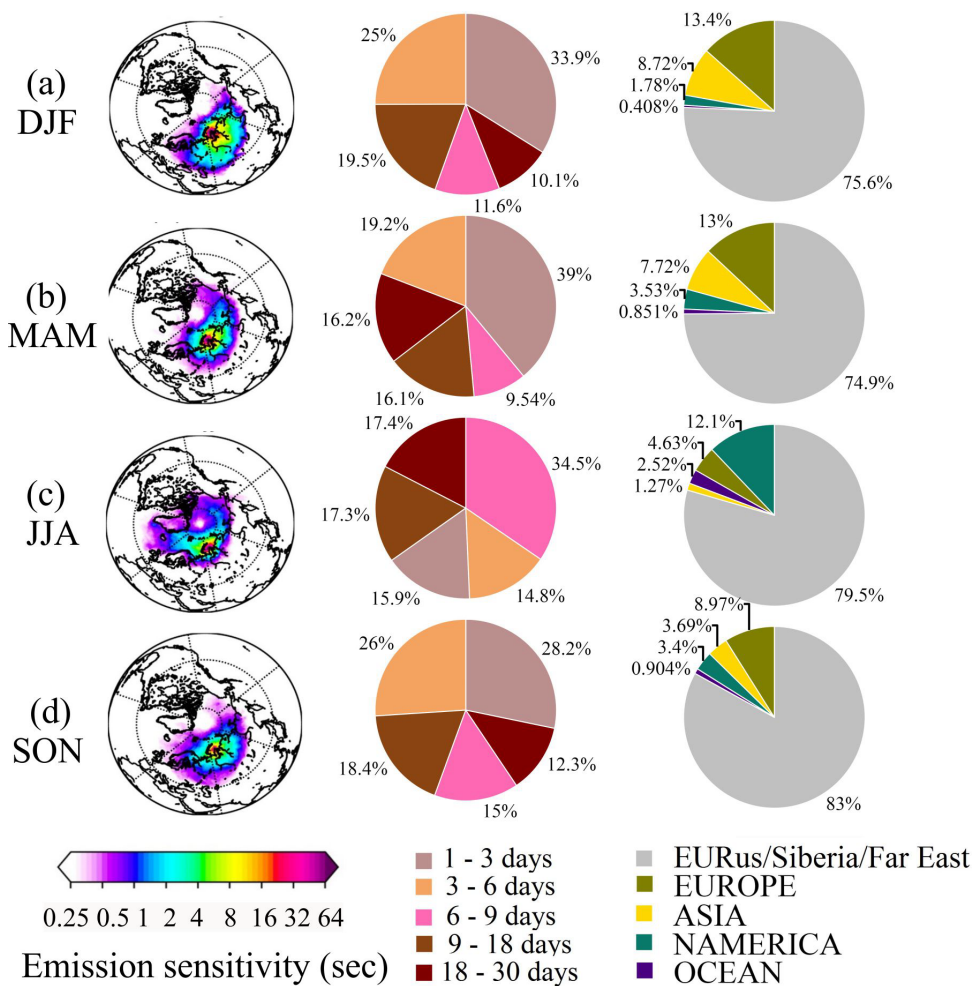
Vertical cross-sections of modelled BC in Bely Station



1116

1117 **Figure 8.** Vertical cross-sections of modelled BC for 2019-2022. Solid and dotted violet lines
1118 represent modelled daily surface BC and *eBC*, respectively. Their levels correspond to the right
1119 (secondary) axis (also in violet). Boundaries between the cold (November- April) and warm (May-
1120 October) are indicated by thick vertical black lines.

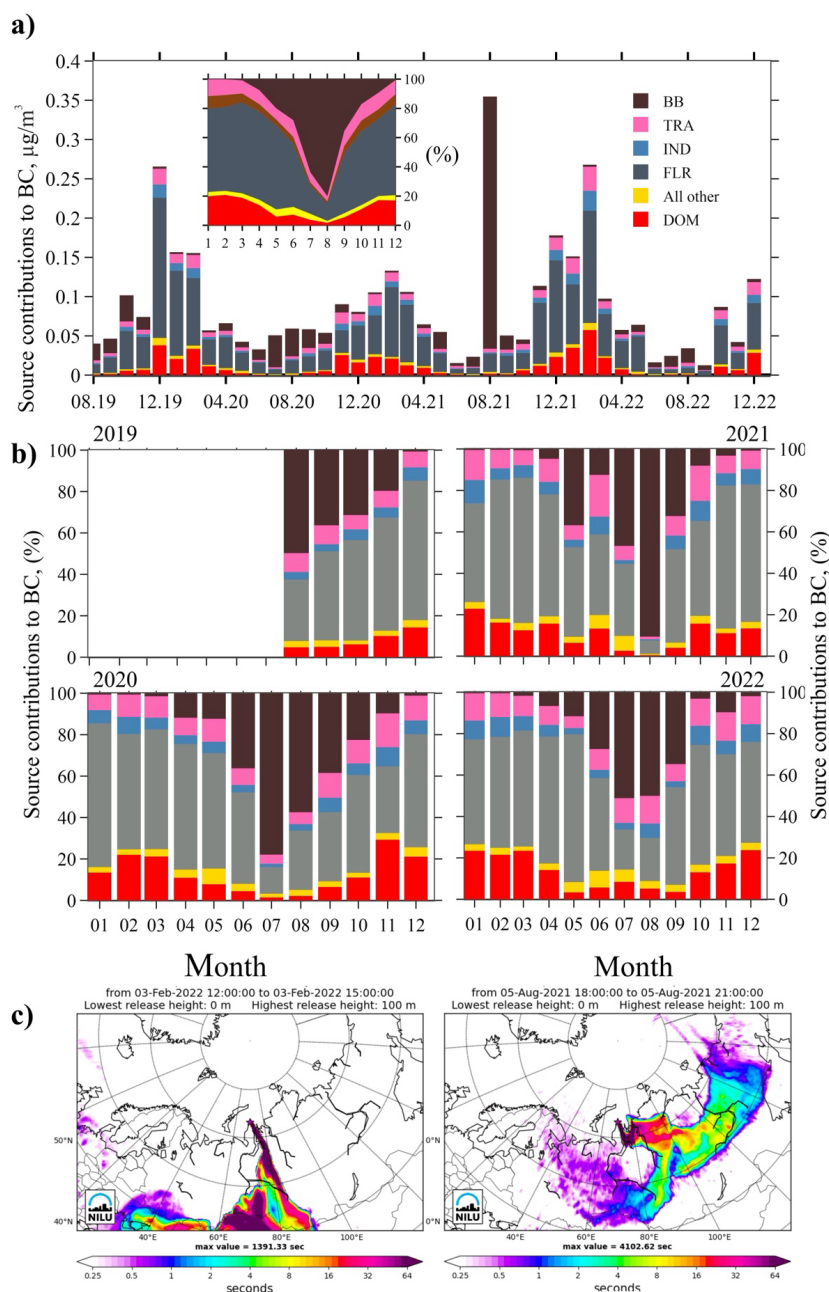
1121



1122

1123 **Figure 9.** (a-d) Season average footprint emission sensitivity, mean age contribution of emissions
 1124 from different day-periods back in time and each region contribution to surface concentration of
 1125 BC.

1126



1127

1128 **Figure 10.** (a) Timeseries of monthly mean contribution from different emission source types to
 1129 surface BC concentrations for the study period. (b) Percentage of monthly mean source
 1130 contributions for each year. Residential and commercial (DOM), biomass burning (BB),
 1131 transportation (TRA), industrial combustion and processing (IND), gas flaring (FLR), and All
 1132 others sources were adopted from ECLIPSEv6 and CAMS GFAS. (c) FES for 3 February 2022 and
 1133 5 August 2021 showing the largest probability of emission origin.

1134



1135 **TABLES & LEGENDS**

1136

1137

1138 **Table 1.** Statistics of light - absorption coefficients; EC, OC, eBC_{AET} , and eBC mass concentration;
 1139 absorption Angstrom exponents (AAE) for the study period, cold and warm periods. Mean± standard
 1140 deviation (1σ), 1st and 3rd Q quartile (25th and 75th percentiles).

Variable	August 2019 - December 2022				cold (November-April)				warm (May-October)			
	mean±sd	median	1 st Q	3 rd Q	mean±sd	median	1 st Q	3 rd Q	mean±sd	median	1 st Q	3 rd Q
$b_{abs}(880)$ (Mm^{-1})	0.5±0.9	0.3	0.1	0.6	0.7±0.7	0.5	0.22	0.9	0.4±0.9	0.2	0.09	0.4
$b_{abs}(520)$ (Mm^{-1})	0.9±1.6	0.4	0.2	1	1.2±1.2	0.8	0.38	1.5	0.6±1.8	0.3	0.1	0.6
$b_{abs}(370)$ (Mm^{-1})	1.2±2.4	0.6	0.3	1.4	1.6±1.6	1.1	0.52	2.1	0.9±2.8	0.4	0.2	0.9
EC ($\mu g m^{-3}$)	0.03±0.03	0.02	0.01	0.05	0.05±0.03	0.04	0.02	0.06	0.02±0.03	0.02	0.01	0.03
OC ($\mu g C m^{-3}$)	0.45±0.3	0.4	0.3	0.5	0.4±0.2	0.4	0.3	0.5	0.5±0.4	0.4	0.3	0.6
* eBC_{AET} ($ng m^{-3}$)	65±83	36	16	80	84±90	57	25	115	53±158	23	10	45
* eBC ($ng m^{-3}$)	29±54	13	5	34	44±47	29	12	59	19±57	8.0	4	17
$AAE_{370/950}$	0.96±0.6	0.95	0.7	1.19	0.94±0.4	0.95	0.74	1.1	0.98±0.8	0.95	0.6	1.3
$AAE_{370/520}$	1.0±1.5	0.93	0.4	1.52	0.88±1	0.89	0.49	1.2	1.16±1.9	1.0	0.3	2.0

1141 * eBC_{AET} is defined in section 2.2.

1142 ** eBC is defined in section 3.2.

1143